

# Morphology and Composition of the Helix Nebula

R.B.C. Henry<sup>1</sup>

Department of Physics & Astronomy, University of Oklahoma, Norman, OK 73019;

henry@phyast.nhn.ou.edu

K.B. Kwitter<sup>1</sup>

Department of Astronomy, Williams College, Williamstown, MA 01267;

kkwitter@williams.edu

and

R.J. Dufour<sup>2,3</sup>

Department of Space Physics & Astronomy, Rice University, Houston, TX 77005-1892;

rjd@rice.edu

Received \_\_\_\_\_; accepted \_\_\_\_\_

To appear in *The Astrophysical Journal*

---

<sup>1</sup>Visiting Astronomer, Kitt Peak National Observatory, National Optical Astronomy Observatories, which is operated by the Association of Universities for Research in Astronomy, Inc. (AURA) under cooperative agreement with the National Science Foundation.

<sup>2</sup>Visiting Astronomer, Palomar Observatory, operated by the California Institute of Technology.

<sup>3</sup>Guest Observer, International Ultraviolet Explorer Satellite, which was operated by NASA, ESA, and the SERC.

## ABSTRACT

We present new narrow-band filter imagery in  $H\alpha$  and  $[N\ II]\ \lambda 6584$  along with UV and optical spectrophotometry measurements from 1200Å to 9600Å of NGC 7293, the Helix Nebula, a nearby, photogenic planetary nebula of large diameter and low surface brightness. Detailed models of the observable ionized nebula support the recent claim that the Helix is actually a flattened disk whose thickness is roughly one-third its diameter with an inner region containing hot, highly ionized gas which is generally invisible in narrow-band images. The outer visible ring structure is of lower ionization and temperature and is brighter because of a thickening in the disk. We also confirm a central star effective temperature and luminosity of 120,000K and  $100L_{\odot}$ , and we estimate a lower limit to the nebular mass to be  $0.30M_{\odot}$ . Abundance measurements indicate the following values:  $He/H=0.12\ (\pm 0.017)$ ,  $O/H=4.60\times 10^{-4}\ (\pm 0.18)$ ,  $C/O=0.87\ (\pm 0.12)$ ,  $N/O=0.54\ (\pm 0.14)$ ,  $Ne/O=0.33\ (\pm 0.04)$ ,  $S/O=3.22\times 10^{-3}\ (\pm 0.26)$ , and  $Ar/O=6.74\times 10^{-3}\ (\pm 0.76)$ . Our carbon abundance measurements represent the first of their kind for the Helix Nebula. The S/O ratio which we derive is anomalously low; such values are found in only a few other planetary nebulae. The central star properties, the super-solar values of He/H and N/O, and a solar level of C/O are consistent with a  $6.5M_{\odot}$  progenitor which underwent three phases of dredge-up and hot bottom burning before forming the planetary nebula.

*Subject headings:* planetary nebulae: individual (NGC 7293) – stars: evolution

## 1. Introduction

The Helix Nebula (NGC 7293) is one of the best known of all planetary nebulae (PN). Its nearby location ( $d \sim 213$  pc; Harris et al. 1997) and large angular size (angular diameter  $\sim 960$  arcmin) make it particularly attractive for detailed investigations of PN structure, morphology and composition. The well known ionized double ring of this evolved PN is surrounded by a massive molecular envelope which has also been studied intensively (Healy & Huggins 1990; Kastner et al. 1996; Cox et al. 1998). Recent observations with HST have showcased “cometary globules” extending radially outward from the nebular center, which presumably represent ablation from dense clumps that survived the PN event (O’Dell & Handron 1996). Observations by Meaburn et al. (1998) also imply that the likeliest origin of these knots is the copious and dusty wind from the red giant precursor.

The central star of the Helix, a DAO white dwarf (Napiwotzki & Schönberner 1995), is one of the hotter and more massive PN central stars. Recent temperature and mass determinations by Górny, Stasińska, & Tylenda (1997) yield  $T_{\text{eff}} = 117,000\text{K}$  and  $M_* = 0.93M_{\odot}$ . Abundances in the Helix have been studied by Hawley (1978), by Peimbert & Torres-Peimbert (1987) and by Peimbert, Luridiana, & Torres-Peimbert (1995). In the latter two papers it is classified as a Peimbert Type I PN, exhibiting enhanced N and He abundances. These composition enhancements accord with predictions that Type I PN arise from the presumably rare massive end of the PN progenitor spectrum. In addition, observations of the molecular envelope indicate significant C I, implying that the Helix is also C-rich (Bachiller et al 1997; Young et al. 1997). This suggests that the third dredge-up has occurred.

To further our understanding of this uniquely accessible object, we have undertaken a detailed study combining spatially-resolved spectrophotometry at three locations with narrow-band, flux-calibrated imaging to create a unified chemical composition model of the

Helix. Our modelling efforts have been guided by O’Dell’s (1998) interpretation that the main body of the Helix is better represented by a thick disk rather than by a ring. The model nebulae which we construct are constrained by new surface photometry in  $H\alpha$  and  $[N\ II]\ \lambda 6584$ . Abundance determinations follow the procedure employed in Henry, Kwitter, & Howard (1996) and Kwitter & Henry (1996; 1998) and are carried out by combining Final-Archived IUE spectral data for three positions in the nebula with ground-based optical spectrophotometry of the same positions.

In the next section we present a description of data acquisition and reduction of the photometric and spectroscopic observations. In §3 we present our geometrically-tuned models for the Helix as well as the details of our abundance determinations. Section 4 contains a comprehensive discussion of the Helix and speculations about its progenitor star, while a summary is given in §5.

## 2. Observations and Reductions

### 2.1. Imagery

The imagery observations of NGC 7293 were taken on the night of 1988 December 2 UT using a focal reducing camera and Tektronix 800×800 CCD on the Palomar 1.5m telescope. The camera, developed by J. Hester, covers a 16-arcminute field at a resolution of 1.2'' per pixel. The sky was photometric during the observations and the seeing was estimated to be  $\sim 2\text{--}3''$ . Five images were taken through filters isolating  $H\alpha$ ,  $[NII]\ \lambda\ 6584$ , and  $[SII]\ \lambda 6717+31$  emission lines, along with line-free continuum bands (100 Å FWHM) around 6450Å and 7230Å. Details of the filters and exposure times are given in Table 1A. In addition to these primary images, a series of flat-fields, as well as appropriate exposure dark frames, were taken of an illuminated dome screen through each of the five filters at the

beginning and end of the night.

The images were processed in the usual manner for nebular CCD data using IRAF<sup>4</sup>. Each of the five images was dark-subtracted and flat-fielded; then average sky levels were determined and subtracted. Photometry of ten unsaturated stars in the field was done on each of the images and used to determine scale factors for subtracting the combination of the two continuum images from each of the three emission line (+continuum) images. This produced images of the nebula in the light of the emission lines of  $H\alpha$ ,  $[NII] \lambda 6584$ , and  $[SII] \lambda 6717+31$  only with most stars and (very weak) nebular continuum removed<sup>5</sup>.

Figure 1 shows our  $H\alpha$  image (without continuum subtraction) with the aperture locations for the UV and optical spectroscopy discussed below noted. The ground-based (KPNO) spectroscopy enabled us to calibrate the three emission line images to absolute surface brightness in the lines. The three KPNO slit locations were mapped onto the continuum-subtracted images and counts through each of the apertures extracted. These were compared to the absolute emission line fluxes from the spectra and calibration constants were derived for each image (in  $\text{ergs}/\text{cm}^2/\text{sec}/\text{pixel}$ , where each pixel has an area of  $1.44 \text{ arcsec}^2$ ). The agreement among the three locations between the counts and the spectral fluxes was good; the rms errors in the constants for the three positions were 12% for  $H\alpha$ , 4% for  $[NII]$ , and 14% for  $[SII]$ .

---

<sup>4</sup>IRAF is distributed by the National Optical Astronomy Observatories, which is operated by the Association of Universities for Research in Astronomy, Inc. (AURA) under cooperative agreement with the National Science Foundation.

<sup>5</sup>We acknowledge that the  $H\alpha$  image is slightly contaminated by light from  $[NII] \lambda 6548$  passing through the blue side transmission wings of the filter, but such contamination amounts to only a few percent for the worst cases when the  $[NII]$  line is comparable to  $H\alpha$  in strength.

## 2.2. Spectrophotometry

### 2.2.1. *UV Data*

The UV spectra were taken with the IUE satellite by R.J.D. during two observing runs in 1990-1991. UV slit locations and orientations for positions A, B, and C are shown with ovals in Fig. 1, while the same information for the optical data discussed below are shown with rectangles. Positions A and B were chosen in order to study the brightened emission in the NE nebular section, while position C coincided with the bright SW region. We obtained SWP and LWP spectra for positions A, B, and C. The slit position angle was  $309^\circ$  for A and C and  $322^\circ$  for B. All spectra are low dispersion and were taken with the large aperture ( $21''.7 \times 9''.1$ ). These data were later reprocessed as part of the IUE Final Archive<sup>6</sup> from which our measurements were taken. Table 1B lists the spectra along with their integration times. As an example of the UV data, Figs. 2A,B display the SWP and LWP spectra of position B, where some significant lines are identified.

### 2.2.2. *Optical Data*

The optical data were obtained at KPNO during 7-9 December 1996 UT with the 2.1m telescope plus the Goldcam CCD spectrometer. The three slit positions were chosen so as to produce maximum overlap with the three IUE positions described above. We employed the Ford  $3K \times 1K$  CCD chip with  $15\mu$  pixels. We used a  $5''$ - wide slit that extended  $285''$  in the E-W direction, with a spatial scale of  $0''.78/\text{pixel}$ . Using a combination of two gratings,

---

<sup>6</sup>Spectra in the Final Archive have been systematically and uniformly re-processed by IUE staff using the NEWSIPS algorithms, and represent the best available calibration of these data.

we obtained spectral coverage from 3700-9600Å with overlap from  $\sim 5750 - 6750\text{\AA}$ . For the blue, we used grating #240 in first order, blazed at 5500 Å, with a WG345 blocking filter. Wavelength dispersion was 1.5 Å/pixel ( $\sim 8$  Å FWHM resolution). For the red, grating #58, blazed at 8000Å was used in first order with an OG530 blocking filter. This yielded 1.9 Å/pixel ( $\sim 10$  Å FWHM resolution). The usual bias and twilight flat-field frames were obtained each night, along with HeNeAr comparison spectra for wavelength calibration and standard star spectra for sensitivity calibration. A summary of the observational details is presented in Table 1C.

The optical observations were made at three positions previously observed with the IUE and which are indicated in Fig. 1. Since the position angle of the Goldcam slit is fixed at  $90^\circ$  while the IUE slit position angle is not (cf. Figure 1), the quality of the overlap varies with IUE position angle; we note also that because of the 2:1 relative slit widths, the largest possible overlap of the Goldcam slit onto the IUE slit is  $\sim 50\%$ . Considering slit position angles and widths of the two data sets, we estimate the spatial overlap to be around 31%.

The original images were reduced in the standard fashion using IRAF. Employing tasks in the *kpnoslit* package, these two-dimensional spectra were converted to one dimension by extracting a specific section along the slit. Since the chip is thinned, it produces interference fringes visible in the red. In our red spectra the fringes appear at the  $\pm 1\%$  level at  $\sim 7500\text{\AA}$  and increase in amplitude with increasing wavelength:  $\pm 1.5\%$  at 8000Å,  $\pm 4.5\%$  at 8500Å,  $\pm 6\%$  at 9000Å. However, even at their worst, *i.e.*, at  $\sim 9500\text{\AA}$ , the longest wavelength we measure, the fringe amplitude reaches only about  $\pm 7\%$ . Internal quartz flats were taken at the position of each object both before and after the object integrations in anticipation of removing the fringes during data reduction. As it turned out, however, more noise was introduced in this process than was removed; we therefore decided to leave the fringes

untouched, and to accept this additional uncertainty in our line intensities longward of  $\sim 7500\text{\AA}$ . Our reduced optical spectra for position B are shown in Figures 2C,D, where again we have marked lines of interest.

### 2.2.3. Line Strengths

Strengths of all optical and UV lines were measured using *splot* in IRAF and are reported in Table 2A. Fluxes uncorrected for reddening are presented in columns labelled  $F(\lambda)$ , where these flux values have been normalized to  $H\beta=100$  using our observed value of  $F_{H\beta}$  shown in the third row from the bottom of the table. These line strengths in turn were corrected for reddening by assuming that the relative strength of  $H\alpha/H\beta=2.86$  and computing the logarithmic extinction quantity  $c$  shown in the penultimate line of the table. Values for the reddening coefficients,  $f(\lambda)$ , are listed in column (2), where we employed Seaton’s (1979) extinction curve for the UV and that of Savage & Mathis (1979) for the optical.

Because of the imperfect spatial overlap between the optical and IUE observations, a final adjustment was made by multiplying the IUE line strengths for positions A and B by a merging factor that was determined from the theoretical ratio of the He II lines  $\lambda 1640/\lambda 4686$ . (Since He II  $\lambda 1640$  was unobserved at position C, no correction was made and we list the merging factor as unity.) The calculation of the merging factors is described in detail in Kwitter & Henry (1998), and their values are listed in the last row of Table 2A.

The columns headed  $I(\lambda)$  list our final, corrected line strengths, again normalized to  $H\beta=100$ . Uncertainties in line intensities were ascertained by compiling a list of line ratios with values set by atomic constants. Table 2B shows the theoretical values of the line ratios in column 2 followed by observed ratios and percent differences in the next six columns. We



note that these line ratios span the optical spectrum. If we allow for the fact that [Ne III]  $\lambda 3968$  is problematic because of contamination by H $\epsilon$  and the [S III] near infrared lines suffer from atmospheric absorption and emission, we conclude that all optical and near infrared line strengths above 10% of H $\beta$  have uncertainties of  $\pm 10\%$ , lines weaker than that have uncertainties of  $\pm 20\%$ , UV lines are uncertain by  $\pm 25\%$ , and the [S III] lines in the near infrared are uncertain by more than 50%. A few line strengths which we feel are particularly problematic are indicated with colons in Table 2A.

### 3. Results

Our two principal goals in this study are to: (1) use our imagery of the Helix to examine its gross physical properties including its morphology; and (2) derive accurate chemical abundances using our UV and optical emission line measurements at three positions in the nebula. We discuss these two analyses in the following three subsections.

#### 3.1. Image Analysis - Density and Ionization Variations

Since the line-of-sight (LOS) reddening to the Helix Nebula is small, the H $\alpha$  surface brightness at any point,  $S_{H\alpha}$ , is proportional to the square of the electron density,  $N_e$ , along the LOS path through the ionized medium in that direction:  $S_{H\alpha} \propto \int N_e^2 dl$ . While the constant of proportionality involves atomic data and the nebular filling factor, in a real nebula the density varies along the LOS. Nonetheless, for a first approximation, we can make the oversimplification that the LOS through each point in the nebula has a constant density and filling factor, and then use the square root of the H $\alpha$  surface brightness as an indication of the spatial *variation* in density across the nebula. Fig. 3 is a contour map of  $\sqrt{S_{H\alpha}}$  normalized to unity in the center of the the nebula. The contours show an elliptical

appearance with the highest regions of surface brightness “density” located NNE and SSW of the central star (along PA’s of  $\sim 20^\circ$  &  $215^\circ$ , respectively). Relative to the central “plateau” of the nebula, the “density” enhancements for the NNE and SSW bright rims are  $1.6\times$  and  $1.5\times$ , respectively. As is evident in Fig. 1, these bright rims are also where our slit positions B and C are located. In addition, a hand-drawn fit to the contours in our Fig. 3 yields an ellipse with a major axis along  $PA=32\pm 5^\circ$  and an inclination of  $28\pm 10^\circ$ .

While developing this paper we became aware of two notable studies of the Helix Nebula recently completed. The first, by Meaburn et al. (1998; hereafter M98), deals primarily with the motions and nature of the cometary knots in the central regions of the nebula. However, they also present a global model of the nebula consisting of a torus (+expanding lobes) containing the bulk of the bright knots, inclined  $37^\circ$  with respect to the plane of the sky around an axis with  $PA=14^\circ$ . The second, by C. R. O’Dell (1998; hereafter O98), is a global imagery and long-slit spectroscopy study of the Helix with similarities to our project in its spatial coverage and scientific goals. However, our two papers differ in imagery in that our study employs the red lines of  $H\alpha$ ,  $[N\ II]$ , and  $[S\ II]$ , while O98 use the blue-green lines of  $He\ II$ ,  $H\beta$ , and  $[O\ III]$ . Regarding the true geometrical structure of the Helix Nebula, O98 argues that “the ring is actually a disk” –namely a *filled* torus inclined  $21^\circ$  with respect to the plane of the sky around an axis oriented with  $PA=30^\circ$ .

Our  $H\alpha$  imagery of the Helix agrees best with the “filled disk” model of O98. This is illustrated in Fig. 4, which shows an inclined “surface map” view of the  $\sqrt{S_{H\alpha}}$  contour map shown in Fig. 3 (where north is to the bottom right and east is to the top right). In this representation, it is clear that the central part of the nebula consists of a “plateau” in  $H\alpha$ , rising well above the sky background. Figs. 3 and 4 support the filled disk model of O98, who explained that this morphology is in contrast to the one usually drawn from ordinary images taken in low-excitation lines such as  $[N\ II]$  and  $[S\ II]$ , since the inner region

is dominated by highly ionized material and thus is not visible. While this inner plateau is flat to  $\pm 10\%$  or so in  $\sqrt{S_{\text{H}\alpha}}$  (density), we also confirm the slight systematic drop in the  $\text{H}\alpha$  surface brightness at the interface of the inner ring at distances between 2-3 arcmin from the star.

The signal-to-noise for our calibrated  $\text{H}\alpha$  and  $[\text{N II}] \lambda 6584$  images is excellent and permits the construction of an  $[\text{N II}] \lambda 6584/\text{H}\alpha$  *ratio* image showing the ionization structure of the nebula in  $\text{N}^+$  relative to  $\text{H}^+$  at a spatial resolution better than  $2''$ . This result is shown in Fig. 5 for the full  $16'$  field (left image) and for an  $8'$  enlarged area around the northern rim (right image). Four distinctly different ionization zones in the nebula are apparent: (a) a nearly circular high ionization inner zone for which the ratio is  $0.35 \pm 0.13$ ; (b) an extended elliptical region with major axis along  $\text{PA} \approx 135^\circ$  where generally the ratio is  $\sim 1.3 \pm 0.4$ , but with many “plumes” having lower  $[\text{N II}]/\text{H}\alpha$  values; (c) “rims” in the NE and SW directions defining the outer boundary of the elliptical region where the line ratio is highest (2.2-2.6); and (d) the outer nebular region which shows a slightly higher ratio than the central zone but also with larger variations (0.4-0.8) appearing as smoothly-varying wavy structures.

A comparison of Fig. 5 with an LW2 filter ISOCAM map (Cox et al. 1998; plate 1), where the latter is dominated by molecular hydrogen emission from dense globules with neutral cores and ionized surfaces similar to the photodissociation region morphology seen in some Galactic H II regions, strongly suggests that the rims we see in zone c correspond to material associated with the nebular ionization front. However, while the appearance of the NNE and SSW rims in our  $[\text{N II}]/\text{H}\alpha$  ratio greyscale map is similar to the LW2 ISOCAM image, many of the structures (separated clumps) seen in the LW2 image in the SSE part of the nebula are not apparent in our ratio map. This suggests that the stellar wind and ionization parameter are stronger in the SSE (and NNW) parts of the nebula,

producing a thinner ionization front at those locations and correspondingly lower [N II] surface brightness on the neutral globules.

Another very apparent, even striking, feature of our [N II]/H $\alpha$  ratio map is the appearance of many radial “plumes” seen as elongated structures with lower ratio values crossing the full expanse of the ring in many places. Similar structures are evident in the [O III] $\lambda$ 5007/H $\beta$  ratio map of O98. We interpret these plumes as extensions of the “cometary knot” (CK) structures (O’Dell & Handron 1996) seen in the interface between the high ionization central region and the ring. O’Dell & Burkert (1997) present convincing arguments that the CK are the artifacts of finger-like density-enhanced structures formed by Rayleigh-Taylor instabilities arising from the ionization boundary as it progresses outward into the neutral material ejected from the red giant progenitor of the PN. M98 presented detailed images of the CK in the central regions of the nebula in H $\alpha$  + [N II] along with a detailed kinematical model for the ablated flow of ionized material from the heads of the CK. Such flows are slightly supersonic and form a 3D bow shock cylinder around the CK. Such a flow around the CK in the central disk of the nebula, or similar neutral dusty globules in the outer thicker disk, will have enhanced local emission in [N II], and [O III] compared to H I. M98 also noted that some of the CK had definite absorption in their tails, suggesting that the ablated material is dusty.

The plumes that are observed throughout the thick outer disk of the Helix in [N II] (and [O III]) can thus be explained as enhanced emission from ablated flows of ionized material from neutral globules in the shell. The right panel of Figure 5 shows details of these features in the northern part of the ring, which appear as parabolic “bow shock”-like structures with bright heads when they are studied in high contrast [N II] or [O III] (O98) images or better, in [N II]/H $\alpha$  ratio grey-scaled images where surface brightness effects of the surrounding nebula are minimized. The heads of some of these plumes also

appear in Fig 3C of M98 (bottom left part where the ring brightness begins to grow high), which suggest that they are the same physical phenomena as the CK, only that they are immersed in the denser and lower-ionization ring. While it is possible that darker insides of the CK could be due to dust obscuration by elongated neutral globules, it is more likely due to bright rims expected from looking at a 3D bow shock structure extending nearly along the plane of the sky.

### 3.2. Whole Nebula Model

While on the sub-arcsecond scale the Helix Nebula is frightfully complex with density (and possibly temperature) inhomogeneities, our imagery permits us to further test the proposed geometries of M98 and O98 by developing photoionization models of assorted geometries for the nebula. Thus, we now consider the  $H\alpha$  surface brightness and  $[N II]/H\alpha$  distributions for the Helix. To study this, four radial cuts originating at the central star and extending outward by  $600''$  were made through the  $H\alpha$  and  $[N II]/H\alpha$  images shown in Figs. 1 and 5 for position angles  $24^\circ$ ,  $135^\circ$ ,  $209^\circ$ , and  $315^\circ$ . The cuts at position angles  $24^\circ$  and  $209^\circ$  were made specifically to intersect our spectroscopic positions B and C, respectively, and are each  $5''$  in width. The cuts at  $135^\circ$  and  $315^\circ$  are  $50''$  in width and were made for the purpose of sampling the smoother ring material away from positions B and C. The results are presented in Fig. 6, where the upper panel is a plot of  $H\alpha$  surface brightness in units of  $10^{-15}\text{ergs/cm}^2/\text{s/arcsec}^2$  versus distance from the central star in arcseconds for the cuts at the four position angles. The lower panel shows the value of the intensity ratio of  $[N II] \lambda 6584$  relative to  $H\alpha$  as a function of distance. Radial distances represented in each curve of both panels have been deprojected according to the position angle (PA) of the cut by multiplying each radial coordinate by  $\left\{ \cos^2(\text{PA} - 22^\circ) + \frac{\sin^2(\text{PA} - 22^\circ)}{\cos^2(30^\circ)} \right\}^{1/2}$ . We have assumed a disk inclination with respect to the sky plane of  $30^\circ$  around an axis whose

position angle is  $22^\circ$ . (Note that these angles are roughly averages of values derived by M98 and O98 quoted in §3.1.) Each cut is shown with a line of normal width and types defined in the legend for the specific position angle of the cut. Also shown with bold solid and dashed lines are model results which will be discussed below.

The position of the brightened ring of the Helix appears clearly between  $200''$  and  $300''$  from the central star, as seen by the broad rise in  $H\alpha$  surface brightness for all four position angles at this distance. The cuts at  $24^\circ$  and  $209^\circ$  show additional emission due to the presence of the brightened rims corresponding respectively to our spectroscopic slit positions B and C (see Fig. 1).

In order to interpret the data in Fig. 6 we have calculated two separate models to approximate the data: one corresponding to the cuts along position angles  $135^\circ$  and  $315^\circ$ , which we designate as model 135/315, and another corresponding to position angles  $24^\circ$  and  $209^\circ$ , designated as model 24/209. Notice that the first directional pair lie along a line passing through the central star and extending  $600''$  in each direction, while the second pair lie nearly along a straight line passing through the central star roughly orthogonal to the first pair and including positions B and C. Both models are represented in Fig. 6 with bold lines, with the line type defined in the legend.

The models were produced in two steps. First, we calculated a spherical photoionized model nebula using the code CLOUDY version 90.04 (Ferland 1990), where the program specifically tabulated the volume emissivities of  $H\alpha$  and  $[N\ II]\ \lambda 6584$  as functions of distance from the central star. We then integrated these emissivities along lines-of-sight spaced at  $10''$  intervals from the central star (see Appendix A for detailed specifics of the line-of-sight calculation) to produce the  $H\alpha$  surface brightnesses and  $[N\ II]/H\alpha$  ratios displayed in Fig. 6. Note that in converting the linear distance in the photoionization model to arcseconds we assume a distance to the Helix Nebula of 213 pc (Harris 1997). Variable

parameters in the complete model included central star temperature and luminosity, and nebular composition, density, filling factor, and morphology. In calculating these models we initially assumed a spherical nebula for our line-of-sight calculations but soon found that we could not simultaneously model the observed  $H\alpha$  and  $[N\ II]/H\alpha$  profiles. Thus, we began experimenting with the disk morphology proposed by O’Dell by varying the line-of-sight thickness of the nebula as a function of distance from the central star, assuming that the nebular disk plane is coincident with the plane of the sky (recall that the observations have been deprojected).

The final models displayed in Fig. 6 for 135/315 and 24/209 both employed a blackbody central star effective temperature of 120,000 K, consistent with the value of 117,000K found by Górny, Stasińska, & Tylenda (1997) and a luminosity of  $100\ L_{\odot}$ , which is similar to the number found by Méndez, Kudritzki, & Herrero (1992). The gas phase chemical abundances were set at the values derived later in §3.3, except in the case of nitrogen, which was set at  $1/3$  of its derived value in order to avoid overproducing  $[N\ II]$ . This discrepancy is currently unresolvable. Since we believe that the nitrogen abundances derived at positions A, B, and C below are reasonably precise, the fault must lie here with our whole-nebular models. These models apparently have the tendency to produce too much  $[N\ II]$  per unit of emission measure, forcing us to reduce the nitrogen abundance in order to match the surface photometry. Short of suggesting that all three of the slit positions for our spectroscopy happened to be coincident with nitrogen-rich knots, it is clear that more detailed modelling is necessary to understand this discrepancy. The mass ratio of dust to gas in the models was 0.018, while the filling factor was 0.55. The total gas density in the 135/315 model was  $60\ \text{cm}^{-3}$  throughout. However, in the case of model 24/209, the total density was  $60\ \text{cm}^{-3}$  out to  $250''$ , then rose to a maximum of  $125\ \text{cm}^{-3}$  at  $315''$ , and finally returned to  $60\ \text{cm}^{-3}$  at  $395''$ . This density profile was required to match the  $H\alpha$  and  $[N\ II]/H\alpha$  behavior in Fig. 6. Additionally, in the LOS integration of each of the final models, the

disk thickness ( $Z$ ) relative to its diameter ( $D$ ) was 0.33 from the center out to  $200''$ , then gradually increased to 0.66 at  $275''$ , and returned to 0.33 at  $310''$  in an attempt to imitate O'Dell's model shown in his Fig. 7.

The model results displayed in Fig. 6 provide a reasonable, although not perfect, fit to the observed profiles. In the top panel, model 135/315 (bold solid line) is a good fit to the corresponding  $H\alpha$  data for all but the outermost region of the nebula. In the bottom panel we see that the  $[N II]/H\alpha$  prediction for this model is good out to about  $300''$ , but rises above the observed line by roughly 50% beyond  $400''$ , primarily because of the predicted fall-off in  $H\alpha$  emission at this location, and suggesting that the model Strömgren edge is actually located at a greater distance. However, efforts to correct for this, such as altering the gas density distribution or the stellar luminosity, resulted in an unacceptable deterioration in the  $H\alpha$  predictions in the vicinity of the ring ( $200''$ - $400''$ ).

Turning to model 24/209 (bold dashed line), the general shape of the observed  $H\alpha$  profiles, including the larger rise between  $200$ - $400''$  corresponding to our spectroscopic positions B and C (see Fig. 1), is matched but with a 35% overprediction at around  $230''$ . In the lower panel, model 24/209 provides a nice fit to the observations except for the predicted low ratios beyond  $400''$ . As noted above, the heightened emission between  $200$ - $400''$  was reproduced by raising the total gas density within this region. Doing this, however, caused the location of the ionization front to move inward, causing a drop in emission in both panels beyond  $400''$  for model 24/209. Attempts to move the front out resulted in unacceptably smaller peaks in both panels in the  $200''$ - $400''$  region. Finally, the X symbols in Fig. 6 correspond to values derived from our spectral data in Table 2, where positions A, B, and C are in order of increasing distance from the central star. These data are reasonably consistent with the model as well as the imagery, with the exception of the  $[N II]/H\alpha$  value for position C.



Fig. 7 provides additional support for our models but also indicates some trouble spots. The solid and dashed lines show model predictions for He II  $\lambda 4686$ , [O II]  $\lambda 3727$ , and [O III]  $\lambda 5007$ , all relative to  $H\beta$  and as a function of distance from the central star in arcseconds. Again, the X symbols represent our spectral observations, which should be compared with model 24/209. We have also added spectral results from O98 in order to obtain some constraints on the inner region of the nebula. His observations are shown with horizontal lines bounded by vertical bars, where the line centers correspond to positions of his slit centers and the line lengths indicate the spatial extent of his spectral extractions along the slit. His slit position angle was  $356^\circ$ , and thus his observations should be compared with model 135/315.

We see in the top panel that He II is observed to be strong close to the central star but falls off to near zero at an angular distance of  $\sim 250''$ . This is nicely reproduced by the models, where the strong He II has been produced by reducing the LOS thickness of the nebula, which increases the relative amount of  $\text{He}^{+2}$  to  $\text{H}^+$  along the LOS, and thus the ratio of associated line strengths goes up. In fact, we take the very strong  $\lambda 4686/H\beta$  as an indication that the nebula is flat and not spherical for exactly this reason. In the middle and bottom panels, we see that qualitatively our models reproduce the [O II] and [O III] observations: a low level of [O II] beginning near the central star with higher levels farther out, and the reverse behavior occurring for [O III]. Quantitatively, however, while [O II]/ $H\beta$  and [O III]/ $H\beta$  are well matched by the models in the inner and outer nebular regions, respectively, the model fails to reproduce [O II]/ $H\beta$  beyond  $200''$  and [O III]/ $H\beta$  inside of  $200''$  by as much as a factor of two in each case. The problem could be resolved if a generally lower level of oxygen ionization were present across the nebula, but trials with lower stellar temperatures and higher gas densities caused unacceptable changes in  $\text{H}\alpha$  and [N II] profiles in Fig. 6. We conclude that there are details of the nebular morphology and/or density structure which are unaccounted for in our calculations, but testing more

sophisticated regimes is beyond the scope of this paper.

The ionization structures of He and O, electron temperature and density behavior for the photoionization models associated with models 135/315 and 24/209, along with disk thickness profiles are shown in the five panels of Fig. 8. The top two panels track fractional ionization for relevant ions of He and O across each model nebula, and since our final LOS models are highly flattened, these panels closely represent the behavior in ionization across the nebula in the plane of the sky. Notice that in the vicinity of the central star the gas is dominated by  $\text{He}^{+2}$  and  $\text{O}^{+3}$ , consistent with O'Dell's empirical assessment. Our models also support his finding of electron temperatures in excess of 20,000 K in this same region, as shown in the third panel. O'Dell suggests that these high temperatures are generated by photoelectric heating by dust, a point supported by our photoionization models which include photoelectric effects that contribute close to 96% of the heating in the  $\text{He}^{+2}$  region. Note also that our model [O III] temperatures near positions A, B, and C are quite consistent with those derived in the next subsection and shown here with X symbols. The ionization structure of the 24/209 model is radially compressed relative to the 135/315 model, the result of the density enhancement centered around  $250''$  in the former model and appearing as the broad bump in the fourth panel. This density structure produces a more optically thick nebula beginning in this region, consuming the ionizing photons within smaller volumes. Finally, the bottom panel in Fig. 8 shows values of disk thickness (Z) relative to diameter (D) and may be thought of as an edge-on profile of the Helix Nebula. The bump between 200 and  $300''$  of course corresponds to the brightened ring region of the Helix.

In conclusion, our disk model calculations for the Helix Nebula, inspired by O98 and produced by combining photoionization and LOS models, is consistent with much available imagery and spectrophotometric data, in particular those data for  $\text{H}\alpha$  surface brightness,

and the profiles of [N II] and He II relative to hydrogen emission. Also, ionization structure, electron density and temperature structure, and the edge-on profile all fit with observations, as do the inferred stellar properties. On the other hand, while the models do a good job of reproducing the qualitative behavior for [O II] and [O III], they overproduce emission in nebular regions where these lines respectively dominate. We emphasize that our modeling efforts here are only intended to test the viability of O’Dell’s model of the Helix, and our model is not necessarily unique. Such a claim would require a more extensive exploration of parameter space, an exercise which is beyond the scope of this paper. However, if we assume the model’s validity for the time being, the model suggests that the Helix is generally a filled disk with highly ionized material in the inner section which often appears in images as a void. The brightened ring results from a thickening of the disk along the line-of-sight, while the regions corresponding to our slit positions B and C are locations of density enhancements and are thus additionally brightened. We shall return to a consideration of our model results in §4.

### 3.3. Empirical Abundances

Abundances of He, C, N, O, Ne, S, and Ar at positions A, B, and C were derived by combining our spectra with a hybrid abundance method developed and employed in Henry, Kwitter, & Howard (1996), and Kwitter & Henry (1996; 1998). The heart of the method is the use of a photoionization model to improve results from a five-level atom routine. Briefly, we use a merged set of UV and optical line strengths and derive an initial set of nebular abundance ratios. We next construct a nebular model which is tightly constrained by several important observed diagnostics, and then calculate a second set of abundances based upon the output linestrengths of the model. The ratio of the actual model input abundances to the abundances inferred from model output provides a correction factor

which is then applied to the original set of inferred abundances to determine the final set.

The above procedure can be expressed analytically for the abundance of one element X as follows:

$$X = \left\{ \sum^{\text{obs}} \frac{I_\lambda}{\epsilon_\lambda(T_e, N_e)} \right\} \cdot \text{icf}(X) \cdot \xi(X). \quad (1)$$

$I_\lambda$  is the measured intensity of a spectral feature produced by an ion of element X,  $\epsilon_\lambda(T_e, N_e)$  is the energy production rate per ion of the spectral feature  $\lambda$ ,  $\text{icf}(X)$  is the ionization correction factor, i.e. the ratio of the total abundances of all ions of X to the abundance sum of observable ions, and  $\xi(X)$  is the model-based correction factor alluded to above. We now describe our procedural steps in greater detail.

Emission lines used for calculating the ion abundance ratios inside the curly brackets are He I  $\lambda 5876$ , He II  $\lambda 4686$ , [O II]  $\lambda 3727$ , [O III]  $\lambda 5007$ , [N II]  $\lambda 6584$ , C III]  $\lambda 1909$ , [Ne III]  $\lambda 3869$ , [S II]  $\lambda \lambda 6716, 6731$ , [S III]  $\lambda \lambda 9069, 9532$ , and [Ar III]  $\lambda 7135$ . Specific line strengths were taken from Table 2. Values of  $\epsilon$  are calculated using ABUN, which employs a five-level atom routine, using atomic data the sources for which are listed in Table 3A. This program also calculates electron temperatures and densities. Quotients for observable ions are summed together and multiplied by the ionization correction factor (icf), where the ionization correction factors are calculated according to the following prescriptions taken from Kingsburgh & Barlow (1994), with ion symbols, i.e.  $\text{He}^{+2}$ , implying number abundances:

$$\text{icf}(\text{He}) = \frac{\text{He}}{\text{He}^{+2} + \text{He}^+} = 1.0, \quad (2a)$$

$$\text{icf}(\text{O}) = \frac{\text{O}}{\text{O}^{+2} + \text{O}^+} = \frac{\text{He}^+ + \text{He}^{+2}}{\text{He}^+}, \quad (2b)$$

$$\text{icf}(\text{C}) = \frac{\text{C}}{\text{C}^{+2}} = \frac{\text{O}^+ + \text{O}^{+2}}{\text{O}^{+2}} \cdot \frac{\text{He}^+ + \text{He}^{+2}}{\text{He}^+}, \quad (2c)$$

$$\text{icf}(\text{N}) = \frac{\text{N}}{\text{N}^+} = \frac{\text{O}^+ + \text{O}^{+2}}{\text{O}^+} \cdot \frac{\text{He}^+ + \text{He}^{+2}}{\text{He}^+}, \quad (2d)$$

$$\text{icf}(\text{Ne}) = \frac{\text{Ne}}{\text{Ne}^{+2}} = \frac{\text{O}^+ + \text{O}^{+2}}{\text{O}^{+2}} \cdot \frac{\text{He}^+ + \text{He}^{+2}}{\text{He}^+}, \quad (2e)$$

$$\text{icf}(\text{S}) = \frac{\text{S}}{\text{S}^{+2} + \text{S}^{+}} = \left[ 1 - \left( 1 - \frac{\text{O}^{+}}{\text{O}^{+} + \text{O}^{+2}} \cdot \frac{\text{He}^{+}}{\text{He}^{+} + \text{He}^{+2}} \right)^3 \right]^{-0.33}, \quad (2f)$$

$$\text{icf}(\text{Ar}) = \frac{\text{Ar}}{\text{Ar}^{+2}} = 1.87. \quad (2g)$$

Table 3B lists the derived relative ion abundances, uncertainties, and icf’s by position. We note that abundances of high ionization species such as  $\text{He}^{+2}$ ,  $\text{C}^{+2}$ ,  $\text{O}^{+2}$ ,  $\text{Ne}^{+2}$ , and  $\text{Ar}^{+2}$  were calculated using the [O III] temperature, while abundances of  $\text{He}^{+}$ ,  $\text{O}^{+}$ ,  $\text{N}^{+}$ ,  $\text{S}^{+2}$ , and  $\text{S}^{+}$  were determined using the [N II] temperature. As noted below, our [O II] temperatures appear unreliable due to the uncertainty of the [O II]  $\lambda 7325$  measurements, and thus we consistently used [N II] temperatures for the lower ionization species. The uncertainties were determined rigorously by propagating assumed line strength uncertainties (see §2.2.3) through the individual ion abundance calculations, i.e. the factors in curly brackets in Eq. 1, adding all differential contributions in quadrature. Thus, effects of electron temperature uncertainties on the abundances are accurately accounted for. We note, however, that contributions from uncertainty in atomic data were not included in the error analysis. We also caution that the actual uncertainty in the  $\text{C}^{+2}$  abundance at position C is greater than indicated, due to the absence of He II  $\lambda 1640$  at position C, which prohibited the determination of a UV-optical merging factor at that location. It is interesting to note that as distance from the central star increases in going from position A to position C, the abundances of higher ionized species, i.e.  $\text{O}^{+2}$ ,  $\text{Ne}^{+2}$ , and  $\text{S}^{+2}$ , are seen to systematically decrease, while those of  $\text{O}^{+}$ ,  $\text{N}^{+}$ , and  $\text{S}^{+}$  appear to increase, as is expected because of the decreased density of ionizing photons in more distant regions of the nebula.

We thus derive a preliminary abundance for an element by summing the observed ion abundances for that element in Table 3B and then multiplying the sum by the appropriate ionization correction factor.

The final step in our procedure is to multiply the preliminary abundances by a correction factor  $\xi(X)$ , defined as:

$$\frac{\text{true model abundance}}{\text{apparent model abundance}}. \quad (3)$$

The correction factor  $\xi$  is a gauge of the accuracy of the use of the ionization correction factor method for determining abundances and helps correct abundances determined in the traditional method for effects such as charge exchange. The correction factor is determined by using CLOUDY 90.03a (Ferland 1990) to calculate a photoionization model which best reproduces a wide range of observed diagnostic line ratios. The line strength output by the model is then used as input to ABUN to derive a set of abundances, i.e. the *apparent* abundances in eq. 3. These are compared with the input or *true* abundances for the model to yield  $\xi$ . In particular, the photoionization models for this segment of the abundance determinations were calculated for each slit position in order to reproduce as closely as possible the physical conditions observed along the line-of-sight. Our models were constrained by a set of 10 important diagnostic ratios constructed directly from observed line strengths. These 10 ratios are known to describe the physical conditions of a nebula quite well. Our goal for each of the three positions was to match each observed ratio to within 0.10-0.15 dex, consistent with observational uncertainties<sup>7</sup>. We assumed that the central stars were blackbodies and that the nebula had a uniform density with a filling

---

<sup>7</sup>A possible alternative to this method would be to use our model results in the last section to calculate ionization correction factors along lines-of-sight coincident with our three observed positions. However, while the models in §3.2 successfully reproduced most of the observations, they did not match the [O II]  $\lambda 3727$  and [O III]  $\lambda 5007$  emission satisfactorily throughout the nebula. Therefore, we decided to continue using the routine we have used in the three previous papers which are part of this series on PN abundances.

factor of unity.<sup>8</sup> The inner nebular radius was taken to be 0.032 pc for all models, but the outer radius was treated as a free parameter. In several cases the best matches to the observed line strengths were produced by truncating the model inside the Strömgren radius, i.e. the model nebula was matter-bounded. Other free parameters included the stellar luminosity, nebular electron density, and nebular abundances of helium, oxygen, nitrogen, carbon, neon, and sulfur.

Table 4A summarizes our model results; for each position we list logarithmically the observed and model-predicted values for 10 important diagnostic line ratios in the upper section of the table. The first ratio is sensitive to gas-phase metallicity and electron temperature, the second and third to the level of nebular excitation, the fourth and fifth to electron temperature and density, respectively, and the last five to abundance ratios in the order He/H, N/O, S/O, C/O, and Ne/O. The lower section of the table provides important model input parameters: stellar effective temperature ( $T_{\text{eff}}$ ), the log of stellar luminosity  $\log(L)$ , electron density ( $N_e$ ), and the inner and outer nebular radii ( $R_o$  and  $R$ ; values of  $R$  which are less than the Strömgren distance, i.e. matter bounded models, are indicated with a footnote). These are followed by six input abundance ratios. (N.B. We emphasize that these abundance ratios are *not* our final abundances for each object, but are the abundances necessary to produce the best model.)

There are several important points about the model results that require discussion. First, we note that these models represent the best-fit solutions to a specific line-of-sight position within a nebula; they are *not* models of whole planetary nebulae. Model parameters

---

<sup>8</sup>While most PNe are known to have filling factors significantly less than unity, the only measurable quantity affected by the filling factor is the nebular luminosity, a parameter we are not using to constrain our models. Thus, using the same filling factor for all of the nebulae in no significant way influences our abundance results.

were varied to match quantities measured along a single line-of-sight where local conditions may have large effects on the line strengths. Thus, none of the values for these parameters is necessarily the same as the actual one. Rather, whole nebula properties are treated above in §3.2 using our narrow-band filter images.

We draw the reader’s attention to the satisfactory agreement between observation and theory in all line ratios except the one associated with He II/He I for position C, where the model grossly overpredicts the line strength. This ratio is particularly sensitive to nebular excitation, as is the [O II]/[O III] ratio above it. Curiously, we were able to obtain a good match for the latter, as well as all of the other ratios at this position, suggesting that perhaps our measured line ratio is spurious. We note that the strength of the He II/He I ratio at the other two positions is much higher.

The correction factors  $\xi$  derived using our models and eq. 3 are given in Table 4B. Since all but one of the values is less than unity, we conclude that generally the standard abundance method of using a 5-level atom calculation along with an icf results in values which are systematically too large, although never by more than a factor of two in the worst cases.

The one instance in which we deviated from the above procedure was in the case of the sulfur abundance for position A where [S III] was not measured. Here we used the relation between  $S^+$  and  $S^{+2}$  derived by Kingsburgh & Barlow (1994), i.e.  $S^{+2}/S^+ = 4.677 + (O^{+2}/O^+)^{0.433}$ , to obtain an estimate of the  $S^{+2}$  abundance. We then determined a value for  $\xi$  from our model of position A using this same relation, and obtained a value for S/H. We checked the consistency of this method by applying it to positions B and C and found abundances determined in this way to be very consistent with those calculated using the method expressed in eq. 1.

Our final abundance results for the three positions in the Helix are given in Table 5,



where we include our derived values for [O III], [N II], and [O II] electron temperatures<sup>9</sup> and [S II] electron densities. We also show average values for our three positions (with standard deviations), as well as results for the Helix from Peimbert, Luridiana, & Torres-Peimbert (1995), Hawley (1978), and O’Dell (1998), averages for a large sample of PNe by Kingsburgh & Barlow (1994), abundances in Orion (Esteban et al. 1998), and solar abundances from Grevesse, Noels, & Sauval (1996). Uncertainties in all quantities have been determined by estimating contributions from the ionization correction and  $\xi$  factors and adding them together in quadrature along with uncertainties in ion abundances given in Table 3B.

We find the Helix Nebula to have a metallicity somewhat less than solar, as implied by O/H, in agreement with Hawley but not with Peimbert et al. Our average O/H is similar to the value found by Kingsburgh & Barlow (1994) for a large sample of southern PNe as well as for the O/H level found by Esteban et al. (1998) for the Orion Nebula. Also, O/H in the Dumbbell Nebula (NGC 6853), another PN of close proximity, i.e. 240 pc (Harris et al. 1997), is found by Perinotto (1991) to be  $4.1 \times 10^{-4}$ , close to our value for the Helix. We conclude, then, that O/H in the Helix is largely representative of the local ISM level. With a mass of  $6.5 M_{\odot}$  (see §4), the Helix progenitor formed less than 100 million years ago, when the ISM metallicity would have been similar to its current level. Therefore, the agreement between the Helix and local ISM metallicities is not unexpected.

Our carbon abundances in Table 5 are the first of their kind published for the Helix. The uncertainties for carbon are relatively large primarily because of the temperature

---

<sup>9</sup>The [O II] temperatures are significantly different among the three positions and are inconsistent with [N II] temperatures as well as our model predictions. Presumably, this is due to the large uncertainties in our measurements of the  $\lambda 7325$  quartet feature. As noted earlier, we have opted to use [N II] rather than [O II] temperatures to calculate abundances of lower ionization species.

sensitivity of the excitation rate of [C III]  $\lambda 1909$ . Unfortunately, the recombination line C II  $\lambda 4254$  was not observed in the Helix, and thus we were unable to estimate a carbon abundance using a less temperature-sensitive method. Note that the average C/O value quoted pertains to positions A and B only, since no UV-merging factor could be determined at position C. Considering the uncertainties, the values we find for C/O appear consistent with the average PN level of Kingsburgh & Barlow, as well as the values for Orion and the sun. We are therefore unable to state conclusively that carbon is enriched.

Certainly the evidence for nitrogen enrichment is much greater than for carbon enrichment in the Helix. Our average level of 0.54 for N/O is well above both the solar and Orion levels. In fact the Helix fits the definition of a Peimbert Type I PN, with  $N/O \geq 0.5$  and  $He/H \geq 0.12$ .

Our results for Ne/O and Ar/O show consistency with other PNe, i.e. the KB sample, Orion, and marginally with the sun. According to the stellar yields of Woosley & Weaver (1995)  $^{16}\text{O}$ ,  $^{20}\text{Ne}$  and  $^{36}\text{Ar}$  are synthesized by stars within the same general mass range, i.e. stars with birth masses greater than  $15M_{\odot}$ , and thus Ne/O and Ar/O should be roughly the same everywhere in space and time. Since PN progenitors are not expected to alter their inherited values of Ne and Ar (and probably O, unless ON cycling is significant), it is not too surprising that the two ratios should be the same everywhere. Our results seem consistent with that idea.

The main challenge in our abundance results is attempting to understand the origin of the very low S/O value. We find values roughly an order of magnitude below the KB average for PNe, the sun, and Orion. It should be noted that a few objects in the KB sample have levels of S/O similar to ours, and it is clear from the data that these low S/O levels in both the Helix and the KB sample are associated with relatively weak [S II] emission observed in all of these object. Because the  $\xi$  corrections are within 25% of unity, we are

reasonably confident of our abundance method for deriving S in the Helix. Yet, since S and O are both produced in massive stars, the S/O level in a planetary nebula must represent the value which was present in the interstellar medium at the time that the PN progenitor formed. A depressed value of S/O in the ISM could have been present if, shortly before the Helix progenitor formed nearby, an evolved massive star had ejected material which was low in sulfur relative to oxygen. This nucleosynthetic mix is possible if the boundary between stellar core material which is to be ejected and the material which remains behind in the remnant, i.e. the mass cut, is more distant from the center of the massive star than normal (Nomoto et al. 1997). However, such a reduced sulfur level should be accompanied by a similar reduction in argon, yet that is not inferred from our observations. Another possible explanation is that significant amounts of sulfur reside in ionization states above  $S^{+2}$ , i.e. states which we could not observe directly or account for because of physical conditions unrepresented in our models.

In summary, the Helix Nebula appears to be a Type I PN with He and N enrichment and a metallicity consistent with that of the solar neighborhood as measured by other nebulae, although it is lower in metallicity than the sun. The level of carbon relative to oxygen in the Helix seems to be typical of what is seen in local PNe and H II regions, although C/O exceeds the solar value.

#### 4. Discussion

The relative success of our whole-nebula models along with our abundance measurements of the Helix Nebula provide us with an opportunity to assemble a composite picture of the past and present of this nearby planetary nebula. These models suggest a central star of  $T_{\text{eff}}=120,000\text{K}$  and a luminosity of  $100L_{\odot}$ , implying a radius of  $0.02R_{\odot}$ . The values for  $T_{\text{eff}}$  and  $L$  are very similar to published values quoted in the introduction,

while the radius is consistent with the central star classification as a DAO white dwarf (Napiwotzki & Schönberner 1995). Górny et al. (1997) estimate the mass of the central star to be  $0.93M_{\odot}$ , which, when combined with the initial-final mass relation of (Weidemann 1987), suggests a progenitor mass of  $6.5M_{\odot}$ , corresponding to a B5 main sequence star. At its current distance the Helix progenitor would have appeared in our sky with a visual magnitude of 5.5, barely discernible with the naked eye. Its main sequence lifetime is estimated to have been 56 million years, using the information for stellar lifetimes in Schaller et al. (1992). The dynamical age of the nebula is given by Górny et al. as 22,200 years, based upon Harris’ (1997) distance and a linear diameter of roughly 1 pc, implying an old planetary nebula and explaining its relatively low  $H\alpha$  surface brightness.

The results of our whole-nebula models support the disk morphology of the Helix proposed by O98. In this model the Helix Nebula is imagined to be a disk generally 0.33 pc in thickness which is inclined about  $30^{\circ}$  with respect to the plane of the sky around an axis with a position angle of  $22^{\circ}$ . The disk model and the visible presence of a ring of enhanced emission is consistent with the idea of an isotropic wind interacting with and being directed by a remnant red giant envelope which tends to be concentrated in an equatorial plane (see Balick 1987). The inner region of the disk out to a radial distance of 0.2 pc contains hot gas heated mostly by photoelectric heating through dust in which the temperature exceeds 20,000K. This region is also dominated by highly ionized material such as  $He^{+}$  and  $O^{+3}$ , making it appear empty in the light of lower ionization species such as [N II], [O II], [O III], or [S II]. The total density of this region, as well as for the most of the nebula, is estimated to be around  $60\text{ cm}^{-3}$ .

Beyond the inner region between 0.2 and 0.3 pc radially is the bright ring, the assumed interaction site of a fast stellar wind with the previously-ejected red giant envelope (Balick 1987). Here our models indicate that the enhanced emission is explained by a near doubling

of the disk thickness, producing a greater column density of material; an increase in particle volume density in this region is not suggested. However, in the bright regions where our spectroscopic observations were made, the enhanced brightness above the level of the ring is consistent with a density of roughly  $120 \text{ cm}^{-3}$ , i.e. double the surrounding value. The electron temperature in the ring is estimated to be around 9,000-10,000K, where the heating is no longer controlled by photoelectric processes but by photoionization. The ring region is dominated by  $\text{He}^+$ ,  $\text{O}^{+2}$ ,  $\text{O}^+$ , and  $\text{N}^+$ .

Outside of the ring, the ionization level continues to drop, with the ionization front located at around 0.45 pc. Beyond this point, the gas is dominated by neutral atomic species. If we assume a disk radius of 0.6 pc, a total gas density of  $60 \text{ cm}^{-3}$ , a filling factor of 0.55 (inferred from models in §3.2), and a disk thickness of 0.33 pc, we estimate a nebular mass of  $0.30M_{\odot}$ , which constitutes a lower limit, since presumably the nebular gas extends beyond the 0.6 pc distance. Assuming a progenitor birth mass of  $6.5M_{\odot}$  and a stellar remnant mass of  $0.93M_{\odot}$ , this implies that roughly  $5.3M_{\odot}$  of stellar material is currently dispersed or otherwise unobservable.

Finally, to speculate a bit, during its lifetime, the progenitor of the Helix, given its mass, experienced three dredge-up phases (Iben 1995). The first two took place while the star was on the red giant branch and early on the asymptotic giant branch, respectively, and deposited  $^4\text{He}$  and  $^{14}\text{N}$  in the envelope, while the third phase, which occurs late in the AGB phase, is characterized by thermal pulses and would have dredged up  $^{12}\text{C}$  into the atmosphere. To the extent that hot bottom burning occurred, some of the  $^{12}\text{C}$  would have been converted to  $^{14}\text{N}$  during this phase, thus reducing the amount of the former in the envelope. According to stellar evolution models by van den Hoek & Groenewegen (1997), hot bottom burning occurs in AGB stars of masses in excess of  $5M_{\odot}$ . Therefore, the evidence presented here for minimal carbon enrichment and modest nitrogen enrichment is

consistent with the hot-bottom burning prediction, assuming that the Helix progenitor’s mass was  $6.5M_{\odot}$ .

## 5. Summary

We have undertaken a comprehensive study of NGC 7293, the Helix Nebula, a study which had two goals: (1) to learn about the morphology of the ionized nebula; and (2) to determine accurate chemical abundances in the nebula. In the process, we have obtained, and present here, new narrow-band filter imagery as well as UV and optical spectrophotometry extending from around 1200Å to 9600Å.

The first part of the study involved the use of photoionization models coupled with line-of-sight integrations of emissivities from the former in an attempt to reproduce the observed profiles of  $H\alpha$  surface brightness and  $[N\ II]/H\alpha$  ratios. We were able to match our own observations in addition to those of O’Dell (1998) reasonably well. In addition, our new optical spectrophotometry permitted us to estimate the abundances of He, C, N, O, Ne, S, and Ar at three bright points in the nebula. To our knowledge, this is the first time such measurements have been made in the Helix for C and S.

We have arrived at the following results:

1. Our  $H\alpha$  imagery and photoionization models of the Helix Nebula support the disk model proposed by O’Dell (1998), which includes a hot, highly ionized inner region heated largely by photoelectric processes, as well as a cooler, lower-ionization ring region.
2. Our models also support a central star effective temperature of 120,000K and a luminosity of  $100L_{\odot}$ .

3. The visible disk is roughly 1 pc in diameter and 0.33 pc thick, and is tipped with respect to the sky plane by  $30^\circ$  around an axis with position angle of  $22^\circ$ , where these angles agree well with those found by O’Dell and Meaburn et al. (1998). A lower limit to the mass of the visible nebula is  $0.55M_\odot$ .
4. Abundance measurements suggest that the nebula is enhanced in He and N and we confirm its earlier classification as a Type I PN. Within the uncertainties, carbon does not appear to be enriched relative to oxygen, suggesting that hot-bottom burning occurred during the AGB phase of the progenitor’s evolution. The Helix also appears to have an anomalously low sulfur abundance, which is seen in a few other PNe, but is nevertheless difficult to understand currently in light of current nucleosynthesis scenarios.

We would like to acknowledge support from the staff at KPNO and Palomar Observatory, as well as at the IUE. R.B.C.H. and K.B.K thank their respective institutions for travel support to KPNO. R.J.D. and R.B.C.H. are grateful to the University of Oklahoma and Rice University, respectively, for hospitality during visits. R.J.D. wishes to thank J. Hester for use of the WF PFUEI camera on the Palomar 1.5m to obtain the imagery presented here and to NASA/IUE grant NAG5-262 for supporting the original IUE observations. Finally, we would like to thank Bob O’Dell and Ken Nomoto for useful conversations, and an anonymous referee who offered numerous suggestions for improving the paper.

### A. Line-Of-Sight Integration

The observed nebular surface profiles shown in Fig. 6 were modeled in two steps. First, a photoionization model (CLOUDY) using spherical symmetry was calculated by assuming

a set of input nebular and stellar properties. Relevant output volume emissivities as a function of radial distance were then used as input to a separate program written by one of us (R.B.C.H.) which computed line-of-sight intensities at regular points in the nebula.

The program began by computing the pathlength  $S$  through the nebula of angular diameter  $\Theta$  along a given line of sight located at an angular distance  $\alpha$  from the central star<sup>10</sup>. Thus:

$$S = 2 \times \left\{ \Theta^2 - \alpha^2 \right\}^{1/2} \quad (\text{A1})$$

The pathlength  $S$  was then divided into 1000 equal segments, and beginning at the proximal surface of the nebula the program stepped along  $S$  through the gas, and at each point  $s$  added the emissivity contribution appropriate for the radial distance  $r$ :

$$r = \left\{ \alpha^2 + \left( \frac{S}{2} - s \right)^2 \right\}^{1/2} \quad (\text{A2})$$

where  $s$  is the distance within the nebula along the line-of-sight. This calculation was repeated at  $10''$  intervals beginning at the central star and extending outward to the edge of the nebula. Adjustments were made for the empty nature of the region inside the inner nebular edge. However, because the Helix appears to be tipped by only about  $30^\circ$  with respect to the sky plane, the small increase in line-of-sight pathlength which results was ignored.

---

<sup>10</sup>Angular measurements are easily converted to parsecs or kilometers once the distance is known. In our case we assumed a distance to the Helix of 213 pc (Harris 1997).



Table 1A. Summary of Imagery Observations

Date (UT)	Instrument	Filter	$\lambda_o/\Delta\lambda^1$	Exp(sec)
2 Dec 1988	1.5m WF PFUEI	Halpha	6563/15	600
		RC1	6450/104	120
		[NII]	6584/14	900
		[SII]	6730/36	1200
		IRC1	7230/100	240

<sup>1</sup> $\lambda_o$  = central wavelength,  $\Delta\lambda$  = FWHM, both in Å.

Table 1B. Summary of UV Spectrophotometric Observations

Position	Offsets <sup>1</sup>	Date (UT)	Grating	Exp(sec)
A	97E, 171N	3 Oct 1991	SWP42615	31200
		3 Oct 1991	LWP21398	28200
B	92E, 212N	25 Nov 1990	LWP19278	9000
		25 Nov 1990	SWP40195	3600
		25 Nov 1990	SWP40196	14400
C	151W, 269S	4 Oct 1991	SWP42621	25200
		4 Oct 1991	LWP21401	22800

<sup>1</sup>Given in arcseconds in the sky plane (uncorrected for nebular inclination) with respect to the central star. The offsets are for the slit center. Slit position angle for both A and C was 309° and 322° for B.

Table 1C. Summary of Optical Spectrophotometric Observations

Position	Offset <sup>1</sup>	Date(UT)	Grating <sup>2</sup>	Exp(sec)
A	97E, 171N	7 Dec 1996	Red	1800
		8 Dec 1996	Blue	1800
B	92E, 212N	9 Dec 1996	Red	900
		8 Dec 1996	Blue	1200
C	151W, 269S	9 Dec 1996	Red	1800
		8 Dec 1996	Blue	1200

<sup>1</sup>Given in arcseconds in the sky plane (uncorrected for nebular inclination) with respect to the central star. The offsets are for the slit center. The slit position angle in each case was 90°.

<sup>2</sup>Red: KPNO grating #58, blazed at 8000Å; Blue: KPNO grating #240, blazed at 5500Å.

Table 2A. UV & Optical Line Strengths

Line	$f_\lambda$	A		B		C	
		$F_\lambda$	$I_\lambda$	$F_\lambda$	$I_\lambda$	$F_\lambda$	$I_\lambda$
C II $\lambda 1336$	1.41	...	...	7.8	10	...	...
N IV] $\lambda 1485$	1.23	...	...	11	14	...	...
C IV $\lambda 1549$	1.18	...	...	...	...	56	56
He II $\lambda 1640$	1.14	30	57	17	21	...	...
N III] $\lambda 1750$	1.12			9.5	11	38	38
C III] $\lambda 1909$	1.23	37	70	50	63	95	95
[O III] + C II] $\lambda 2325$	1.35	66	123	25	33	65	65
[O II] $\lambda 3727$	0.29	188	188	475	518	718	718
He II + H10 $\lambda 3797$	0.27	...	...	...	...	5.6	5.6
He II + H9 $\lambda 3835$	0.25	...	...	5.9	6.4	7.1	7.1
[Ne III] $\lambda 3869$	0.25	137	137	101	109	97	97
He I + H8 $\lambda 3889$	0.25	21	21	24	26	25	25
He $\epsilon$ + [Ne III] $\lambda 3968$	0.23	71	71	78	84	80	80
He II $\lambda 4026$	0.21	...	...	1.1	1.2	1.6	1.6
[S II] $\lambda 4072$	0.20	...	...	1.5	1.6	1.7	1.7
He II + H $\delta$ $\lambda 4101$	0.19	23	23	22	23	23	23
H $\gamma$ $\lambda 4340$	0.13	46	46	46	47	44	44
[O III] $\lambda 4363$	0.12	3.5	3.5	2.6	2.7	1.7	1.7
He I $\lambda 4471$	0.09	5.1	5.1	5.5	5.6	5.6	5.6
He II $\lambda 4686$	0.04	8.9	8.9	3.3	3.3	0.46	0.46
H $\beta$ $\lambda 4861$	0.00	100	100	100	100	100	100
He I $\lambda 4922$	-0.02	2.2	2.2	1.9	1.9	1.7	1.7
[O III] $\lambda 4959$	-0.03	209	209	168	167	81	81

Table 2A—Continued

Line	$f_\lambda$	A		B		C	
		$F_\lambda$	$I_\lambda$	$F_\lambda$	$I_\lambda$	$F_\lambda$	$I_\lambda$
[O III] $\lambda 5007$	-0.04	714	714	513	507	309	309
[N II] $\lambda 5755$	-0.21	3.2	3.2	6.3	6.0	11	11
He I $\lambda 5876$	-0.23	15	15	19	17	17	17
[N II] $\lambda 6548$	-0.36	81	81	167	150	280	280
H $\alpha$ $\lambda 6563$	-0.36	272	272	318	286	284	284
[N II] $\lambda 6584$	-0.36	250	250	517	465	842	842
He I $\lambda 6678$	-0.38	4.2	4.2	5.5	4.9	4.9	4.9
[S II] $\lambda 6716$	-0.39	3.6	3.6	10	9.2	22	22
[S II] $\lambda 6731$	-0.39	2.6	2.6	7.4	6.6	16	16
He I $\lambda 7065$	-0.44	3.1	3.1	3.4	3.0	3.5	3.5
[Ar III] $\lambda 7135$	-0.45	23	23	31	27	25	25
[O II] $\lambda 7325$	-0.48	6.4:	6.4:	7.1:	6.2:	11	11
[Ar III] $\lambda 7751$	-0.54	6.3	6.3	6.6	5.7	7.1	7.1
[S III] $\lambda 9069$	-0.67	...	...	0.99:	0.81:	4.2:	4.2:
P8 $\lambda 9228$	-0.68	4.1	4.1	...	...	4.0	4.0
[S III] $\lambda 9532$	-0.70	...	...	28:	23:	16:	16:
$\log F_{\text{H}\beta}^{\text{a}}$		-12.90		-12.79		-12.84	
c			0.00		0.13		0.00
merging factor <sup>b</sup>			1.88		0.87		1.00

<sup>a</sup>Ergs/cm<sup>2</sup>/s in our extracted spectra

<sup>b</sup>Factor by which dereddened UV line strengths are multiplied in order to merge them with optical data (see text).

Table 2B. Line Ratios

Ratio	Theory	Observed					
		A	$\Delta^a$	B	$\Delta^a$	C	$\Delta^a$
[Ne III] 3869/3968 <sup>b</sup>	3.32	2.49	25.0	1.60	51.8	1.52	54.2
He I 5876/4471	2.76	2.94	6.5	3.04	10.1	3.04	10.1
[O III] 5007/4959	2.89	3.42	18.3	3.04	5.2	3.81	31.8
[N II] 6584/6548	2.95	3.08	4.6	3.10	5.1	3.01	1.9
He I 6678/4471	0.79	0.82	4.2	0.88	10.8	0.88	10.8
[Ar III] 7135/7751	4.14	3.65	11.8	4.74	14.4	3.52	14.9
P8/H $\beta$ 9228/4861	0.037	0.041	10.8	...	...	0.04	8.1
[S III] 9532/9069	2.48	...	...	28.4	1044	3.81	53.6

$$^a\Delta = \frac{|\text{Observed} - \text{Theory}|}{\text{Theory}} \times 100.$$

<sup>b</sup>The [Ne III]  $\lambda$ 3968 line was corrected for the contribution from H $\epsilon$ .

Table 3A. ABUN: Sources Of Atomic Data

Ion	Data Type <sup>a</sup>	Reference
H <sup>0</sup>	$\alpha_{\text{eff}}(\lambda 4861)$	Storey & Hummer 1995
He <sup>0</sup>	$\alpha_{\text{eff}}(\lambda 5876)^{\text{b}}$	Péquignot et al. 1991
He <sup>+</sup>	$\alpha_{\text{eff}}(\lambda 4686)$	Storey & Hummer 1995
O <sup>+</sup>	$\Omega$	Mendoza 1983 (2-3,4-5); McLaughlin & Bell 1993 (all other transitions)
	A	Wiese, Fuhr, & Deters 1996
O <sup>+2</sup>	$\Omega$	Burke, Lennon, & Seaton 1989 (4-5); Lennon & Burke 1994 (all other transitions)
	A	Wiese, Fuhr, & Deters 1996
N <sup>+</sup>	$\Omega$	Lennon & Burke 1994
	A	Wiese, Fuhr, & Deters 1996
C <sup>+2</sup>	$\Omega$	Berrington et al. 1985
	A	Nussbaumer & Storey 1978; Kwong et al. 1993 ( $\lambda 1909$ only)
Ne <sup>+2</sup>	$\Omega$	Butler & Zeppen 1994
	A	Baluja & Zeppen 1988
S <sup>+</sup>	$\Omega$	Ramsbottom, Bell, & Stafford 1996
	A	Mendoza 1983
S <sup>+2</sup>	$\Omega$	Galavís et al. 1995
	A	Mendoza 1983
Ar <sup>+2</sup>	$\Omega$	Galavís et al. 1995
	A	Mendoza & Zeppen 1983

<sup>a</sup> $\alpha_{\text{eff}}$ =effective recombination coefficient;  $\Omega$ =collision strength; A=transition rate.

<sup>b</sup>Includes collisional effects given by Clegg (1987).

Table 3B. Ion Abundances & Ionization Correction Factors

Ion Ratio	A	B	C
$\text{He}^+/\text{H}^+$	$0.11(\pm 0.015)$	$0.13(\pm 0.016)$	$0.13(\pm 0.016)$
$\text{He}^{+2}/\text{H}^+(\times 10^3)$	$7.89(\pm 0.74)$	$2.97(\pm 0.27)$	$0.41(\pm 0.04)$
icf(He)	1.00	1.00	1.00
$\text{O}^+/\text{H}^+(\times 10^4)$	$0.94(\pm 0.26)$	$2.38(\pm 0.87)$	$3.27(\pm 0.91)$
$\text{O}^{+2}/\text{H}^+(\times 10^4)$	$3.62(\pm 0.86)$	$2.25(\pm 0.30)$	$1.38(\pm 0.20)$
icf(O)	1.07	1.02	1.00
$\text{C}^{+2}/\text{H}^+(\times 10^4)$	$3.74(\pm 6.4)$	$2.52(\pm 2.2)$	...
icf(C)	1.35	2.10	...
$\text{N}^+/\text{H}^+(\times 10^4)$	$0.62(\pm 0.06)$	$1.04(\pm 0.13)$	$1.84(\pm 0.20)$
icf(N)	5.18	1.99	1.43
$\text{Ne}^{+2}/\text{H}^+(\times 10^4)$	$2.04(\pm 0.68)$	$1.43(\pm 0.24)$	$1.29(\pm 0.24)$
icf(Ne)	1.35	2.10	3.37
$\text{S}^+/\text{H}^+(\times 10^7)$	$1.77(\pm 0.35)$	$4.03(\pm 1.1)$	$9.61(\pm 2.1)$
$\text{S}^{+2}/\text{H}^+(\times 10^6)$	...	$1.45(\pm 0.57)$	$1.04(\pm 0.42)$
icf(S)	1.28	1.04	1.01
$\text{Ar}^{+2}/\text{H}^+(\times 10^6)$	$2.90(\pm 0.47)$	$2.88(\pm 0.33)$	$2.66(\pm 0.32)$
icf(Ar)	1.87	1.87	1.87



Table 4A. Observations & Models

	A		B		C	
	Obs	Model	Obs	Model	Obs	Model
$\log (I_{[\text{OII}]} + I_{[\text{OIII}]})/H\beta$	1.06	1.10	1.08	1.01	1.06	1.04
$\log I_{[\text{OII}]} / I_{[\text{OIII}]}$	-0.71	-0.71	-0.12	-0.13	0.24	0.24
$\log I_{\text{HeII}}/I_{\text{HeI}}$	-0.22	-0.22	-0.72	-0.72	-1.57	-0.17
$\log I_{\lambda 4363} / I_{\lambda 5007}$	-2.31	-2.32	-2.27	-2.24	-2.27	-2.22
$\log I_{\lambda 6716} / I_{\lambda 6731}$	0.14	0.14	0.15	0.15	0.14	0.15
$\log I_{\text{He I}}/H\beta$	-0.83	-0.79	-0.76	-0.77	-0.77	-0.78
$\log I_{6584/3727}$	0.12	0.14	-0.047	-0.056	0.069	0.031
$\log I_{6724/3727}$	-1.48	-1.44	-1.52	-1.53	-1.27	-1.27
$\log I_{1909/5007}$	-1.01	-0.99	-0.91	-0.88	...	-0.78
$\log I_{3869/5007}$	-0.72	-0.73	-0.66	-0.67	-0.50	-0.46
Model Input Parameters <sup>a</sup>						
$T_{\text{eff}} (10^3\text{K})$		93		77		100
$\log L/L_{\odot}$		5.2		3.3		1.5
$N_{\text{e}}$		30		30		30
$R_{\text{o}}(\text{pc})$		0.032		0.032		0.032
$R (\text{pc})$		5.9 <sup>b</sup>		1.8		0.41 <sup>b</sup>
$\text{He}/\text{H}$		0.12		0.12		0.12
$\text{O}/\text{H} (\times 10^4)$		5.19		3.33		4.45
$\text{C}/\text{O}$		1.03		0.72		0.72
$\text{N}/\text{O}$		0.71		0.44		0.44

Table 4A—Continued

	A		B		C	
	Obs	Model	Obs	Model	Obs	Model
Ne/O		0.39		0.32		0.31
S/O ( $\times 10^3$ )		3.49		2.63		3.93
Ar/O ( $\times 10^3$ )		11.1		11.4		11.4

<sup>a</sup>These parameter values are those necessary to match line-of-sight observations only. They do *not* necessarily correspond with the real values for the nebula as a whole, simply because conditions along one direction usually do not represent global nebular conditions.

<sup>b</sup>Matter bounded models

Table 4B. Correction Factors ( $\xi$ )

Ratio	A	B	C
He/H	0.96	0.92	0.90
O/H	0.98	0.92	1.00
C/O	0.95	0.67	0.56
N/O	1.14	0.99	0.79
Ne/O	0.70	0.51	0.31
S/O	0.76	0.72	0.73
Ar/O	0.70	0.57	0.56

Table 5. Derived Abundances, Temperatures, & Densities

Ratio	A	B	C	Ave	PLTP <sup>a</sup>	H <sup>b</sup>	O <sup>c</sup>	KB <sup>d</sup>	Orion <sup>e</sup>	Sun <sup>f</sup>
He/H	0.12( $\pm 0.017$ )	0.12( $\pm 0.018$ )	0.12( $\pm 0.017$ )	0.12	0.13	0.19	0.14	0.12	0.10	0.10
O/H( $\times 10^4$ )	4.78( $\pm 1.35$ )	4.36( $\pm 1.27$ )	4.67( $\pm 1.29$ )	4.60( $\pm 0.18$ )	9.12	3.3	4.30	4.78	5.25	7.41
C/O	0.98( $\pm 1.72$ )	0.75( $\pm 0.73$ )	...	0.87( $\pm 0.12$ )	...	...	...	1.15	0.59	0.48
N/O	0.74( $\pm 0.26$ )	0.43( $\pm 0.17$ )	0.44( $\pm 0.18$ )	0.54( $\pm 0.14$ )	>0.39	0.95	0.89	0.47	0.11	0.13
Ne/O	0.39( $\pm 0.21$ )	0.32( $\pm 0.18$ )	0.29( $\pm 0.21$ )	0.33( $\pm 0.04$ )	>0.63	0.80	...	0.26	0.15	0.16
S/O( $\times 10^3$ )	3.57( $\pm 2.0$ )	2.94( $\pm 1.9$ )	3.16( $\pm 1.7$ )	3.22( $\pm 0.26$ )	...	...	...	17.4	28.2	28
Ar/O( $\times 10^3$ )	7.77( $\pm 3.5$ )	6.48( $\pm 3.3$ )	5.97( $\pm 2.9$ )	6.74( $\pm 0.76$ )	8.71	...	...	5.13	5.89	4.47
T <sub>[O III]</sub> ( $\times 10^{-3}$ K)	9.1( $\pm 0.88$ )	9.5( $\pm 0.44$ )	9.4( $\pm 0.46$ )	9.3( $\pm 0.17$ )	10.2	10.7	11.7	...	...	...
T <sub>[N II]</sub> ( $\times 10^{-3}$ K)	9.6( $\pm 0.37$ )	9.7( $\pm 0.53$ )	9.8( $\pm 0.38$ )	9.7( $\pm 0.08$ )	8.2	9.3	9.4	...	...	...
T <sub>[O II]</sub> ( $\times 10^{-3}$ K)	15.2( $\pm 1.3$ )	8.3( $\pm 0.30$ )	9.3( $\pm 0.40$ )	10.9( $\pm 3.0$ )	...	...	...	...	...	...
N <sub>e</sub> (cm <sup>-3</sup> )	<100	<100	<100	<100	100	570	...	...	...	...

<sup>a</sup>Helix abundance results from Peimbert, Luridiana, & Torres-Peimbert (1995)

<sup>b</sup>Helix abundance results from Hawley (1978)

<sup>c</sup>Helix abundance results from O'Dell 1998

<sup>d</sup>Average PN abundances for the complete sample of Kingsburgh & Barlow (1994)

<sup>e</sup>Abundances (gas+dust) for the Orion Nebula from Table 19 of Esteban et al. (1998)

<sup>f</sup>Solar abundances from Grevesse, Noels, & Sauval (1996)

## REFERENCES

- Bachiller, R., Forveille, T., Huggins, P., & Cox, P. 1997, *A&A*, 324, 1123
- Balick, B. 1987, *AJ*, 94, 1641
- Baluja, K.L., & Zeippen, C.J. 1988, *J. Phys. B*, 21, 1455
- Berrington, K.A., Burke, P.G., Dufton, P.L., & Kingston, A.E. 1985, *Atomic Dat Nuc Dat Tab*, 33, 195 635
- Burke, V.M., Lennon, D.J., & Seaton, M.J. 1989, *MNRAS*, 236, 353
- Butler, K., & Zeippen, C.J. 1994, *A&AS*, 108, 1
- Cox, P., Boulanger, F, Huggins, P.J., Tielens, A.G.G.M., Forveille, T., Bachiller, R., Cesarsky, D., Jones, A.P., Young, K., Roelfsema, P.R., & Cernicharo, J. 1998, *ApJ*, 495, 23
- Esteban, C., Peimbert, M., Torres-Peimbert, S., & Escalante, V. 1998, *MNRAS*, 295, 401
- Ferland, G.J. 1990, *Ohio State Univ. Rep.* 90-02
- Galavís, M.E., Mendoza, C., & Zeippen, C.J. 1995, *A&AS*, 111, 347
- Górny, S.K., Stasińska, G., & Tylenda, R. 1997, *A&A*, 318, 256.
- Grevesse, N., Noels, A., & Sauval, A.J. 1996, in *Cosmic Abundances*, ASP Conf. Ser. 99, S.S. Holt & G. Sonneborn, eds, ASP, p.117
- Harris, H.C., Dahn, C.C., Monet, D.G., & Pier, J.R. 1997, in *IAU Symp.* 180, ed. H.J. Habing & H.J.G.L.M. Lamers (Dordrecht: Kluwer), p. 40.
- Hawley, S.A. 1978, *PASP*, 90, 370

- Healy, A.P., & Huggins, P.J. 1990, *AJ*, 100, 511.
- Henry, R.B.C., Kwitter, K.B., & Howard, J.W. 1996, *ApJ*, 458, 215
- Iben, I. 1995, *Physics Reports*, 250, 1
- Kastner, J.H., Weintraub, D.A, Gatley, I., Merrill, K.M., & Probst, R.G. 1996, *ApJ*, 462, 777.
- Kingsburgh, R.L., & Barlow, M.J. 1994, *MNRAS*, 271, 257
- Kwitter, K.B., & Henry, R.B.C. 1996, *ApJ*, 473, 304
- Kwitter, K.B., & Henry, R.B.C. 1998, *ApJ*, 493, 247
- Kwong, V., et al. 1993, *ApJ*, 411, 431
- Lennon, D.J., & Burke, V.M. 1994, *A&AS*, 103, 273
- McLaughlin, B.M., & Bell, K.L. 1993, *ApJ*, 408, 753
- Meaburn, J., Clayton, C.A., Bryce, M., Walsh, J.R., Holloway, A.J., & Steffen, W. 1998, *MNRAS*, 294, 201
- Méndez, R.H., Kudritzki, R.P., & Herrero, A. 1992, *A&A*, 260, 329
- Mendoza, C. 1983, in *IAU Symp. 103, Planetary Nebulae*, ed. D.R. Flower (Dordrecht: Reidel), 143
- Mendoza, C., & Zeippen, C.J. 1983, *MNRAS*, 202, 981
- Napiwotzki, R., & Schönberner, D. 1995, *A&A*, 301, 545.
- Nomoto, K, Hashimoto, M., Tsujimoto, T., Thielemann, F.-K., Kishimoto, N., Kubo, Y., & Nakasato, N. 1997, *Nuclear Phys. A.*, A616, 79c.

- Nussbaumer, H., & Storey, P.J. 1978, A&A, 64, 139
- O'Dell, C.R. 1998, AJ, preprint.
- O'Dell, C.R., & Burkert, A. 1997, in Planetary Nebulae, IAU Symp. 180, H. Habing & H.J.G.L.M. Lamers, eds. (Reidel: Dordrecht), p.332
- O'Dell, C.R., and Handron, K.D. 1996, AJ, 111, 1630.
- Peimbert, M., Luridiana, V., & Torres-Peimbert, S. 1995, Rev. Mex. Astron. Ap., 31, 131.
- Peimbert, M., & Torres-Peimbert 1987 Rev. Mex. Astron. Ap., 14, 450.
- Péquignot, D., Petitjean, P., & Boisson, C. 1991, A&A, 251, 680
- Perinotto, M. 1991, ApJS, 76, 687
- Ramsbottom, C.A., Bell, K.L., & Stafford, R.P. 1996, Atom Dat Nuc Dat Tab, 63, 57
- Savage, B.D., & Mathis, J.S. 1979, ARA&A, 17, 73
- Schaller, G.; Schaerer, D.; Meynet, G.; Maeder, A. 1992, A&AS, 96, 269
- Seaton, M.J. 1979, MNRAS, 187, 73p
- Storey, P.J., & Hummer, 1995, MNRAS, 272, 41
- van den Hoek, L.B., & Groenewegen, M.A.T. 1997, A&A, 123, 305
- Wiedemann, V. 1987, A&A, 188, 74
- Wiese, W.L., Fuhr, J.R., & Deters, R. 1996, J. Chem. Phys. Ref. Data, Monograph #7.
- Woosley, S.E., and Weaver, T.A. 1995, ApJS, 101, 181
- Young, K., Cox, P., Huggins, P.J., Forveille, T., & Bachiller, R. 1997, ApJ, 482, L101.

Fig. 1.— Logarithmic negative greyscale image of the Helix Nebula in  $H\alpha$  with our KPNO (rectangles) and IUE (ovals) slit positions and orientations illustrated. The image was taken on the Palomar 1.5m telescope with a focal-reducing lens system developed by J. Hester.

Fig. 2A.— IUE SWP spectrum of position B. Emission lines of interest are indicated.

Fig. 2B.— Same as 2A but for LWP.

Fig. 2C.— Optical spectrum of position B obtained with the Goldcam spectrograph and blue grating attached to the KPNO 2.1m telescope. Emission lines of interest are marked. Lines marked with an asterisk have components from the night sky, whose effects were difficult to nullify completely. We do not report strengths for these lines nor do we use them in any calculations.

Fig. 2D.— Same as C. but for the red grating.

Fig. 3.— Density contour map of the Helix Nebula made from our continuum subtracted  $H\alpha$  image, where the field is identical to that of Figure 1. The figure shows iso-density contours normalized to the average density of the center of the nebula. Each contour step is in ratio units of  $\pm 0.1$  with a range from 0.5 in the outer parts to 1.6 in the brightest rim area NNE of the central star.

Fig. 4.— A 3D surface representation of the line-of-sight density, where north is to the bottom right and east is to the top right. Note the elevated surface brightness of the center compared to the outer perimeter of the nebula, and relative flatness of that region within the brighter ring of the nebula.

Fig. 5.— Calibrated greyscale ratio map of  $[N\ II]\lambda 6584$  divided by  $H\alpha$  for the Helix Nebula



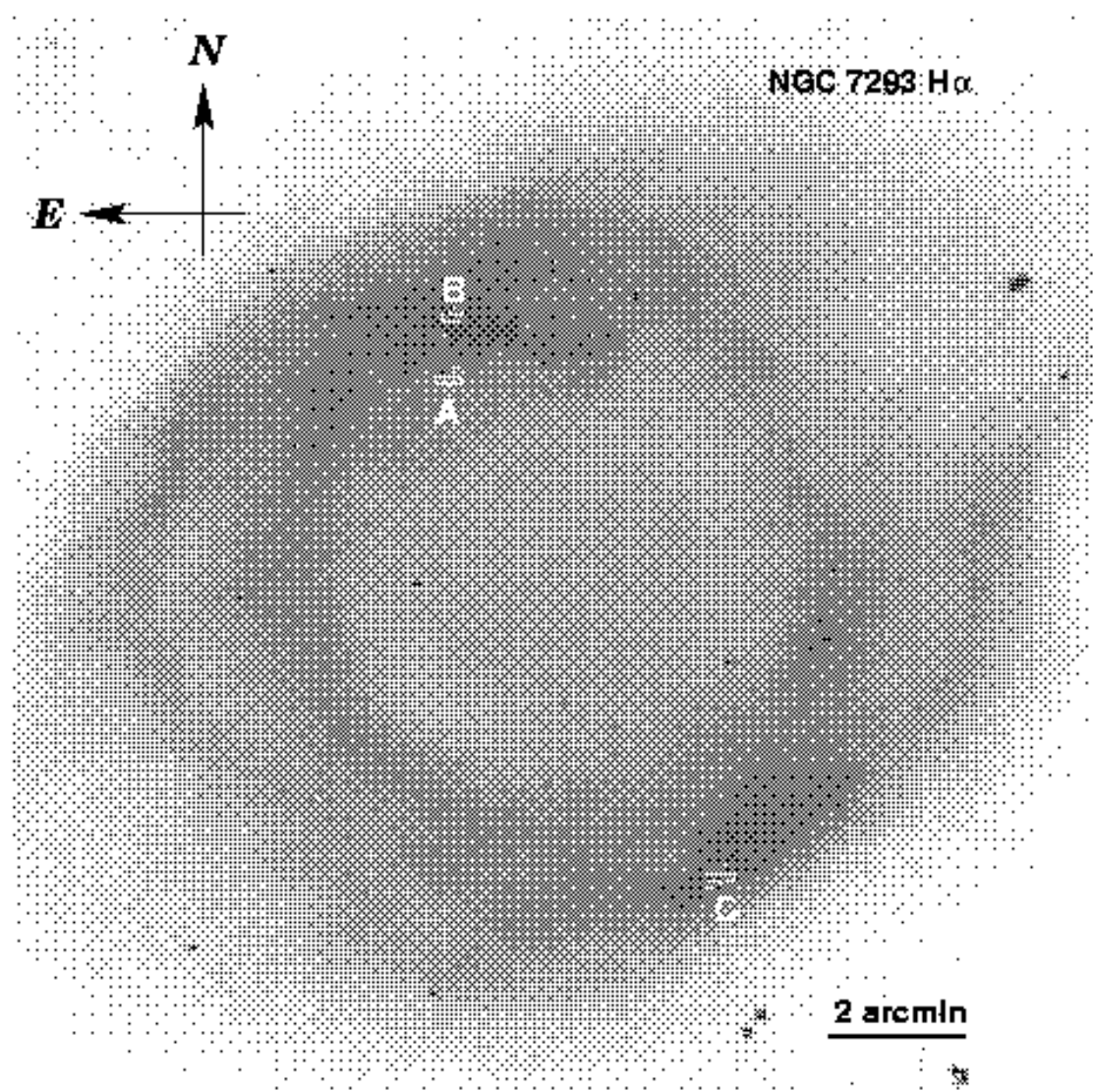
with continuum and stars subtracted. The greyscale is linear, ranging from 0 (white) to 3 (black) for the ratio values. The left panel presents the full  $16'$  field, while the right panel presents an enlarged view of the area around the northern rim of  $8'$ . Note the many “plumes” emanating from knots, where the plumes are bright in [N II] at their heads (dark on our ratio image). See text for discussion.

Fig. 6.— Upper panel:  $H\alpha$  surface brightness in  $10^{-15} \text{ erg cm}^{-2} \text{ s}^{-1} \text{ arcsec}^{-2}$  versus distance from the central star in arcseconds, where  $1'' = 1 \times 10^{-3} \text{ pc} = 3.2 \times 10^{15} \text{ cm}$ , assuming a distance to the nebula of 213 pc. Line type is used to designate position angle of the sample cut, as defined in the legend. These data have been deprojected, as described in the text. The bold lines represent model results described in the text. Values from the spectrophotometric observations reported in §2.2 are indicated with X symbols. Lower panel: same as upper panel but for the intensity ratio [N II]  $\lambda 6584/H\alpha$ .

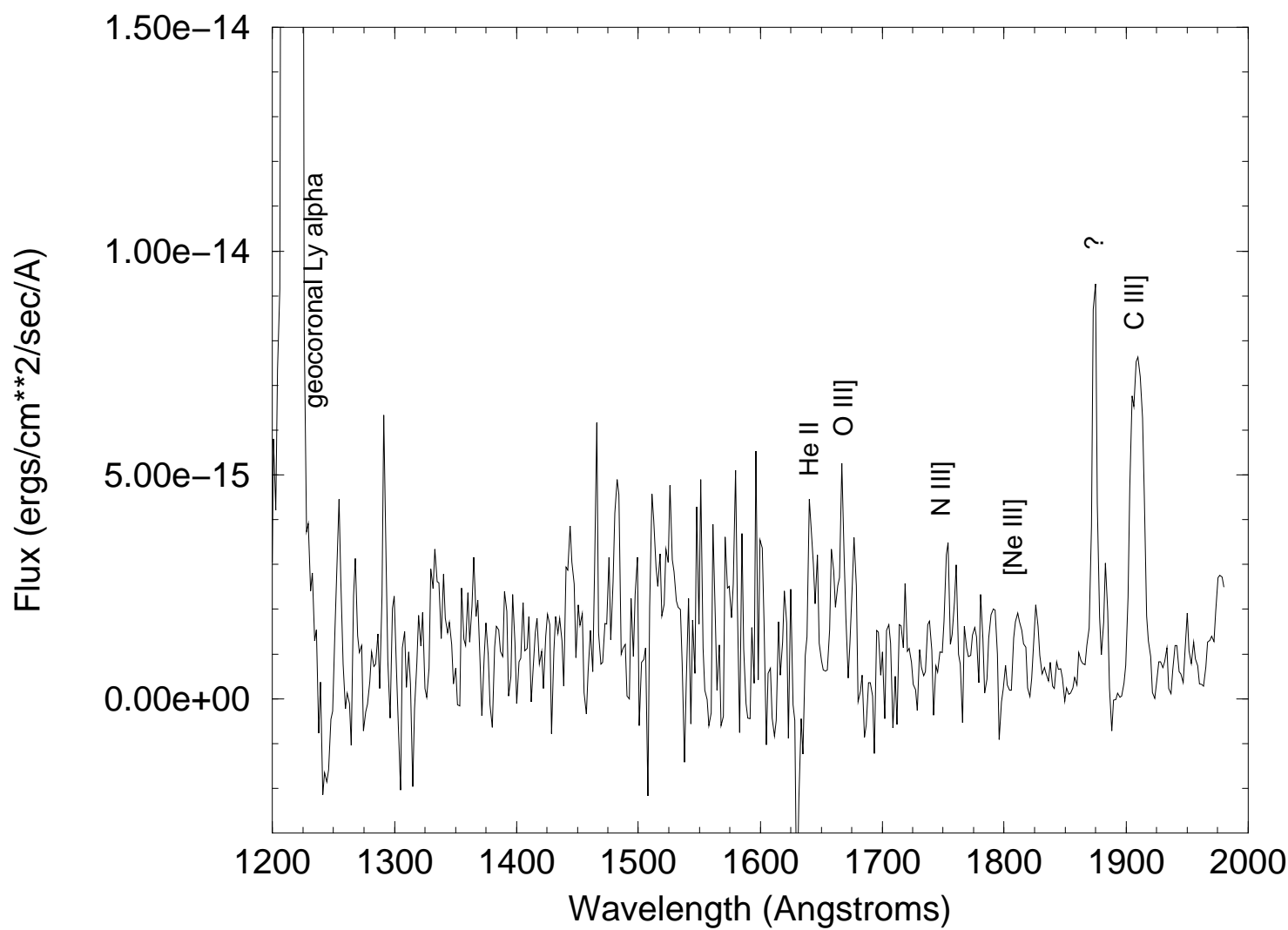
Fig. 7.— A. Predicted intensity ratios of He II  $\lambda 4686/H\beta$  versus distance from the central star in arcseconds for the model simulations of nebular conditions along position angles 135 and 315 degrees (solid line) and 24 and 209 degrees (dashed line). Values from the spectrophotometric observations reported in §2.2 are indicated with X symbols. Spectrophotometric measurements from O’Dell (1998) are shown with short horizontal lines and error bars, where the latter indicate the length along the slit of the extracted spectrum. B. Same as A. but for [O II]  $\lambda 3727/H\beta$ . C. Same as A. but for [O III]  $\lambda 5007/H\beta$ .

Fig. 8.— A. Fractional ionization of the three ions of helium as a function of distance from the central star in arcseconds. The solid line shows the model results for the position angles  $135^\circ$  and  $315^\circ$ , while the dashed line shows the results for position angles  $24^\circ$  and  $209^\circ$ . B. Same as a. but for fractional ionization of oxygen. C. Same as A. but for electron temperature. X symbols give values for [O III] electron temperatures derived in §3.3. D. Same as A. but for electron density. X symbols give values for [S II] electron densities derived in §3.3. E. Same

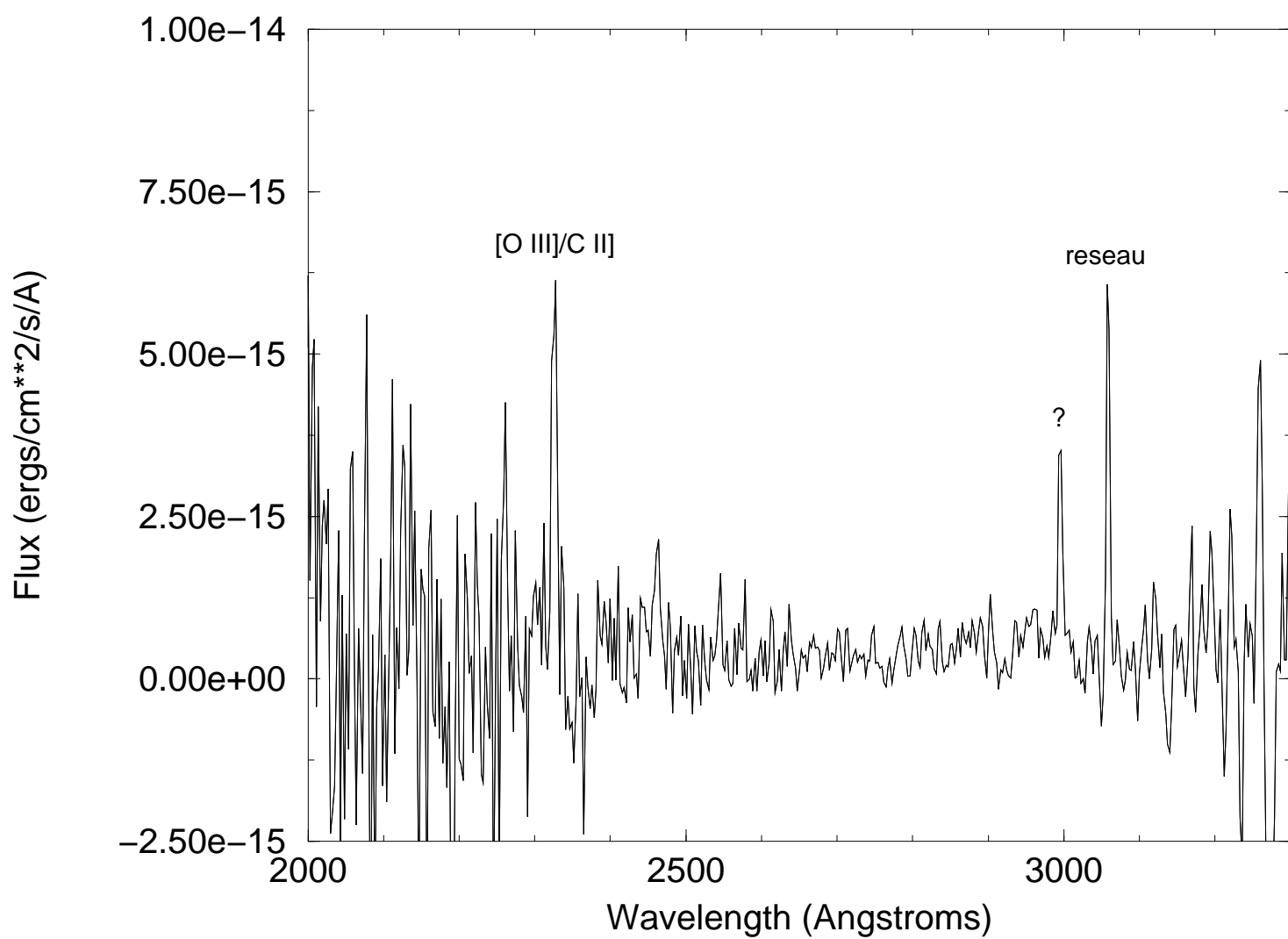
as A. but for the ratio of disk thickness (Z) to diameter (D).



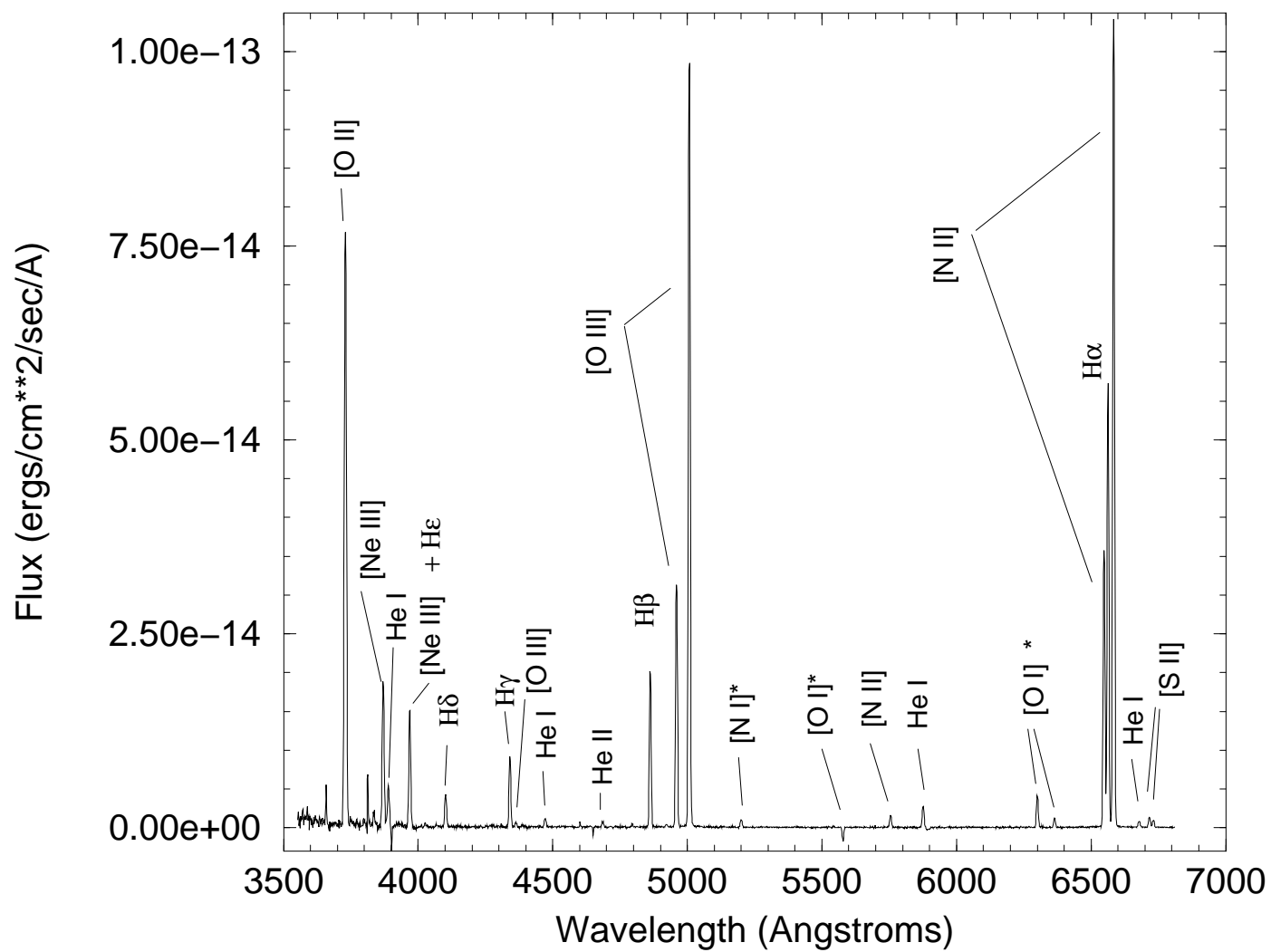
# NGC 7293 Position B



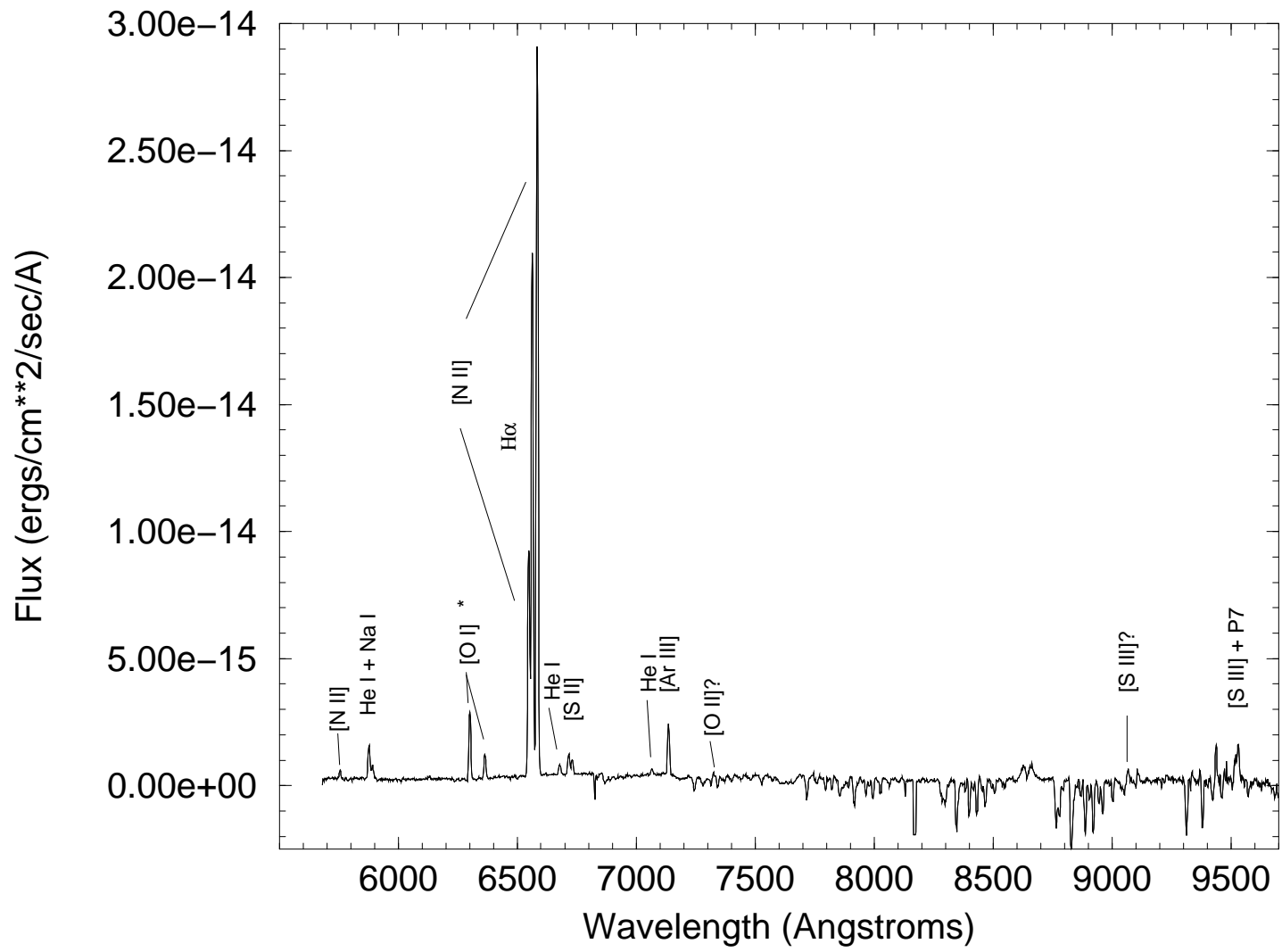
# NGC 7293 Position B

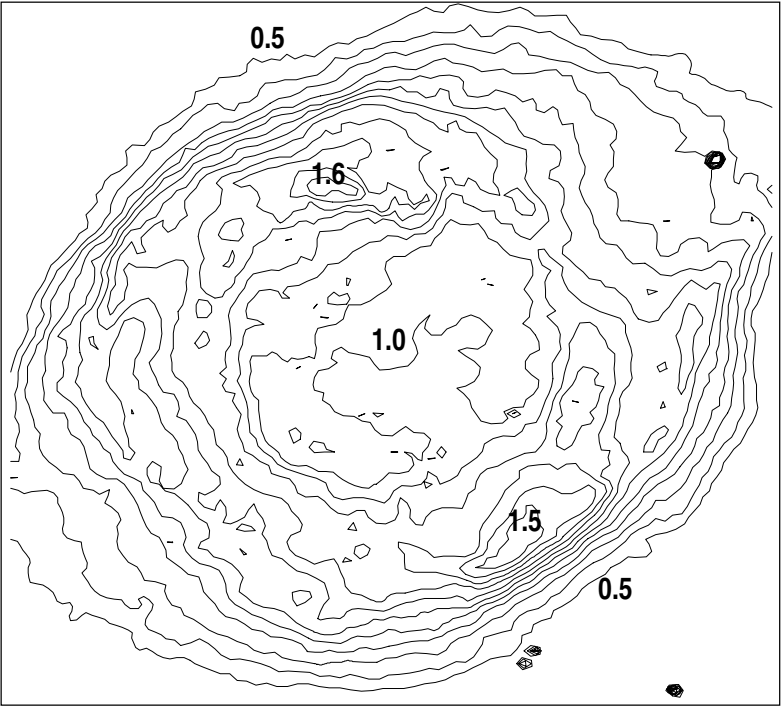


# NGC 7293 Position B



# NGC 7293 Position B







Helix Nebula: L.O.S. Density

